Processing and analysis of HF radar measurements of currents and sea states in the Iroise and Celtic Seas

MERIFIC Deliverable 3.1.4

Actimar :

C. Taillandier
H. Pineau
N. Thomas

Ifremer :

C. Maisondieu

Plymouth University :

G. Lopez
D. Conley

MERiFIC was selected under the European Cross-Border Cooperation Programme INTERREG IV A France (Channel) ï England, co-funded by the ERDF.

The sole responsibility for the content of this report lies with the authors. It does not represent the opinion of the European Communities. The European Commission is not responsible for any use that may be made of the information contained therein.

©

Summary

1 Introduction 2

2 Surface current measurement using WERA HF radars data 2

2.1 Development of the operational DF method for the WERA HF radars data 2

2.1.1 The SORT2RADIAL Processing tool 3

2.1.1.1 MUSIC Algorithm 3

2.1.1.2 Azimuthal processing chain 3

2.2 Comparison of the two methods for the measurement of currents in the Fromveur area 4

2.2.1 East ï West component 5

2.2.2 North - South component 6

2.2.3 Norm of the total velocity vector 6

2.2.4 Comments 7

2.3 Comparison of HF radar measurements with available in situ measurements 8

2.3.1 ADCP PRO2A 9

2.3.1.1 East - West Component 9

2.3.1.2 North ï South Component 10

2.3.1.3 Norm of the total velocity vector 12

2.3.2 ADCP PRO2B 13

2.3.2.1 East - West Component 13

2.3.2.2 North ï South Component 15

2.3.2.3 Norm of the total velocity vector 16

2.3.3 Comments 18

2.4 Statistic indicators for measured surface currents adapted to Marine Renewable Energies applications. 18

2.4.1 Statistics of the space distribution of measured surface currents 19

2.4.2 Space distribution statistics of currents direction 24

2.4.3 Specific analysis around Ushant Island 26

2.4.4 Tides analysis 27

2.4.4.1 Methodology 27

2.4.4.2 Compass roses for currents corresponding to tides with 45, 70 and 95 tidal coefficients. 28

2.4.4.3 Flood and Ebb currents maps for tides with tidal coefficients of 45 and 95 31

2.4.5 Comparison of Beam Forming and Direction finding azimuthal methods 33

3 Sea-states measurement from WERA HF radars: processing and analysis 35

3.1 Significant wave height (Hs) measurement using WERA HF radars 35
3.1.1 Classical empirical method 35
3.1.1.1 Description 35
3.1.1.2 Quality control of radars measurement 35
3.1.1.3 Calibration of the empirical algorithm for the Iroise sea 38
3.1.2 The empirical method adapted to the configuration of the Iroise Sea 41
3.1.2.1 Description 41
3.1.2.2 Quality control of the radar measurements 42
3.1.2.3 Discussions on the results of the modified empirical method 44
3.1.2.4 Testing of modified algorithms on the Plymouth University data sets 47
3.1.3 The empirical method calibrated for the Celtic Sea 49
3.1.3.1 Description 49
3.1.3.2 Quality control of the radar measurements 50
3.1.3.3 Discussion on the results of the modified empirical method 52
3.1.4 Feasibility and validation study of a Barrick's Equation inversion method 53
3.1.4.1 Description 53
3.1.4.2 Nonlinear inversion based on Hisaki formulation 55
3.1.4.3 Comparison of the linearized and empirical methods 56
3.2 Statistics of significant wave height measured by HF radar in the Iroise Sea 60
3.2.1 Data pre-processing 60
3.2.1.1 HF radar sea-states data 60
3.2.1.2 Masking 61
3.2.2 Sea-states statistics in the Iroise Sea 63
3.2.2.1 Mapping of the results 63
3.2.2.2 Detailed analysis at different locations 67
3.3 Statistics of significant wave height measured by HF radar in the Celtic Sea. 68
3.3.1 Data pre-processing 68
3.3.1.1 HF radar sea-state data 68
3.3.1.2 Masking 69
3.3.2 Sea-states statistics in the Celtic Sea 70
3.3.2.1 Mapping the results 70
3.3.2.2 Detailed analysis at different locations 73
4 Conclusions **76**

List of Figures

Figure 1 : SORT2RADIAL Azimutal processing chain..... 4
Figure 2 : Fromveur area and reference measurement point (red dot)..... 4
Figure 3 : Time series for the 2 methods BF (blue) and DF (green), East-West component. . 5
Figure 4 : Scatter plot and Q-Q plot for both methods BF and DF, East-West Component 5
Figure 5 : Time series for the 2 methods BF (blue) and DF (green), North - South component. 6
Figure 6 : Scatter plot and Q-Q plot for both methods BF and DF, North ï South Component6
Figure 7 : Time series for the 2 methods BF (blue) and DF (green), Norm of the total vector.7
Figure 8 : Scatter plot and Q-Q plot for both methods BF and DF, Norm of the total vector ... 7
Figure 9 : Location of the ADCP surveys over the Iroise Sea 8
Figure 10 : Time series of ADCP measured (red) and BF (blue) and DF (green) methods, East-West component 9
Figure 11 : Scatter plot and Q-Q plot for both methods BF (blue) and DF (green) as functions of ADCP measurement, East-West Component 10
Figure 12 : Scatter plot and Q-Q plot comparison of BF and DF methods, East-West Component.....10
Figure 13 : Time series of ADCP measured (red) and BF (blue) and DF (green) methods, North - South component 11
Figure 14 : Scatter plot and Q-Q plot for both methods BF (blue) and DF (green) as functions of ADCP measurement, North - South Component 11
Figure 15 : Scatter plot and Q-Q plot comparison of BF and DF methods, North - South Component.....12
Figure 16 : Time series of ADCP measured (red) and BF (blue) and DF (green) methods, Norm of the total vector 12
Figure 17 : Scatter plot and Q-Q plot for both methods BF (blue) and DF (green) as functions of ADCP measurement, Norm of the total vector 13
Figure 18 : Scatter plot and Q-Q plot comparison of BF and DF methods, Norm of the total vector 13
Figure 19 : Time series of ADCP measured (red) and BF (blue) and DF (green) methods, East-West component 14
Figure 20 : Scatter plot and Q-Q plot for both methods BF (blue) and DF (green) as functions of ADCP measurement, East-West Component 14
Figure 21 : Scatter plot and Q-Q plot comparison of BF and DF methods, East-West Component.....15
Figure 22 : Time series of ADCP measured (red) and BF (blue) and DF (green) methods, North - South component 15
Figure 23 : Scatter plot and Q-Q plot for both methods BF (blue) and DF (green) as functions of ADCP measurement, North - South Component 16
Figure 24 : Scatter plot and Q-Q plot comparison of BF and DF methods, North - South Component.....16
Figure 25 : Time series of ADCP measured (red) and BF (blue) and DF (green) methods, Norm of the total vector 17
Figure 26 : Scatter plot and Q-Q plot for both methods BF (blue) and DF (green) as functions of ADCP measurement, Norm of the total vector 17
Figure 27 : Scatter plot and Q-Q plot comparison of BF and DF methods, Norm of the total vector 18

Figure 28 : space coverage and rate of occurrence of surface current measurement over the period 07/2006 - 08/2011 19
Figure 29 : mean surface current velocity amplitudes over the period 07/2006 - 08/2011 20
Figure 30 : Median value of surface current velocity amplitudes over the period 07/2006 - 08/2011 20
Figure 31 : 99% quantile of surface current velocity amplitudes over the period 07/2006 - 08/2011 21
Figure 32 : Probability of occurrence of velocities higher than 0.25 m/s over the period 07/2006 - 08/2011 21
Figure 33 : Probability of occurrence of velocities higher than 0.5 m/s over the period 07/2006 - 08/2011 22
Figure 34 : Probability of occurrence of velocities higher than 0.75 m/s over the period 07/2006 - 08/2011 22
Figure 35 : Probability of occurrence of velocities higher than 1 m/s over the period 07/2006 - 08/2011 23
Figure 36 : Probability of occurrence of velocities higher than 1.5 m/s over the period 07/2006 - 08/2011 23
Figure 37 : Frequency of occurrence of directions (polar histograms) superimposed with mean velocity amplitude of surface currents over 07/2006 - 08/2011 24
Figure 38 : Frequency of occurrence of directions (polar histograms) superimposed with mean velocity amplitude of surface currents around Ushant Island over 07/2006 - 08/2011 24
Figure 39 : Surface currents compass rose around Ushant Island, 07/2006 - 08/2011 25
Figure 40 : Statistics in the Fromveur strait (Point N°11) over the period 07/2006 - 08/2011. Velocity amplitudes histogram (upper left), directions histogram (upper right), currents compass rose (lower left), currents compass rose for currents > 0.5 m/s (lower right). 26
Figure 41 : Statistics in the North-west of Ushant island (Point N°5) over the period 07/2006 - 08/2011. Velocity amplitudes histogram (upper left), directions histogram (upper right), currents compass rose (lower left), currents compass rose for currents > 0.5 m/s (lower right). 27
Figure 42 : measured currents for tides with tidal coefficient 45 28
Figure 43 : Current compasses for tides with a tidal coefficient of 45 29
Figure 44 : Current compasses for tides with a tidal coefficient of 70 30
Figure 45 : Current compasses for tides with a tidal coefficient of 95 31
Figure 46 : Max of current velocity amplitude for flood (left) and ebb (right) for a tidal coefficient of 45 32
Figure 47 : Max of current velocity amplitude for flood (left) and ebb (right) for a tidal coefficient of 95 32
Figure 48 : Maps of the differences of the annual mean current velocity obtained using DF and BF methods 33
Figure 49 : BF method, statistics in the Fromveur strait (point N°11) : velocity compass and histogram. 33
Figure 50 : DF method, statistics in the Fromveur strait (point N°11) : velocity compass and histogram. 34
Figure 51 : Location of wave buoys used for the analysis 35
Figure 52 : comparison of HF radar and 02911 wave buoy Hs data - October 2009 to July 2010. 36
Figure 53 : comparison of HF radar and 02902 wave buoy Hs data - October 2009 to July 2010. 37

Figure 54 : Calibration curves for the Hs measurement empirical algorithm. 38
Figure 55 : Comparison between radar Hs and 02911 wave buoy Hs before calibration - December 2009.....40
Figure 56 : Comparison between radar Hs and 02911 wave buoy Hs after calibration - December 2009.....41
Figure 57 : comparison of HF radar and 02911 wave buoy Hs data - October 2009 to July 2010 - Modified empirical method.....42
Figure 58 : comparison of HF radar and 02902 wave buoy Hs data - October 2009 to July 2010 - Modified empirical method.....43
Figure 59 : Comparison of Hs measured by the wave buoy 02911 and estimated from radar data using the modified empirical method - December 2009 44
Figure 60 : Comparison between Norgas wave model and buoy 02902 "Ouessant Large"...45
Figure 61 : Norgas model significant wave height compared with radar measurement using classical and modified empirical method at the location "Ouessant Large". 46
Figure 62 : Norgas model significant wave height compared with radar measurement using the classical empirical method at the location "Ouessant Large". 46
Figure 63 : Norgas model significant wave height compared with radar measurement using the modified empirical method at the location "Ouessant Large". 47
Figure 64 : Location of the PU HF Radars and reference wave buoy 47
Figure 65 : Map of Significant wave height measured by the PU HF radars 48
Figure 66 : Comparison of the classical (left) and modified (right) empirical methods with wave buoy data - PU Radar data.....48
Figure 67: Location of the wave buoy used both for calibration and validation of the empirical method. The coordinates of the wave buoy are 50.3422N, -05.6057W.....49
Figure 68 : Calibration curves for the Hs measurement empirical algorithm 50
Figure 69: Comparison between radar Hs and Wave Hub buoy before calibration ï March 2012 to December 2012. 51
Figure 70: Comparison between radar Hs and Wave Hub buoy after calibration ï March 2012 to December 2012. 52
Figure 71: Comparison of HF radar and wave buoy Hs data ï May 2012 ï Modified empirical method. 53
Figure 72 : Wave directional spectrum obtained from nonlinear inversion of the radar data - "Pierres Noires " location - January 15th 2010 midnight 54
Figure 73 : Wave directional spectrum obtained WWIII Norgas wave model - "Pierres Noires " location - January 15th 2010 midnight.....55
Figure 74 : Wave spectra and second order Doppler spectra on October 14th 2009 03:00 - "Les Pierres nNoires". Initial model (upper plot), final model after inversion (lower plot) 56
Figure 75 : Wave spectra and second order Doppler spectra on October 14th 2009 03:00 - "Les Pierres Noires". Initial model (upper plot), final model after inversion (lower plot) 57
Figure 76 : Omnidirectional spectra over the period October 2009 - December 2009, "Pierres Noires" wave buoy (left), modified empirical method (center), linearized inversion SeaView (right).....57
Figure 77 : Significant wave height over the period October 2009 - December 2009, "Pierres Noires" wave buoy, modified empirical method, linearized inversion SeaView. 58
Figure 78 : Significant wave height at the "Pierres Noires" location - comparison between linearized method and in-situ measured data 58
Figure 79 : Significant wave height at the "Pierres Noires" location - comparison between modified empirical method and in-situ measured data.....59

Figure 80 : Peak period over the period October 2009 - December 2009, "Pierres Noires" wave buoy, modified empirical method, linearized inversion SeaView.....59
Figure 81 : Peak period at the "Pierres Noires" location - comparison between linearized method and in-situ measured data 60
Figure 82 : Peak period at the "Pierres Noires" location - comparison between modified empirical method and in-situ measured data 60
Figure 83 : number of valid Hs data per pixel 61
Figure 84 : Mean difference between raw data and filtered data.....62
Figure 85 : Mask based on two first criteria (red pixels are removed) (left). Average Hs for the year 2010 (right) 62
Figure 86 : Final mask using the three criteria (red pixels are removed) (left). Resulting map for the mean Hs for the year 2010. (right). 63
Figure 87 : Mean Hs from radar measurement (October 2009 - June 2011).....64
Figure 88 : Maximum Hs from radar measurement (October 2009 - June 2011) 64
Figure 89 : Hs monthly means for months January to June (October 2009 - June 2011).....65
Figure 90 : Hs monthly means for months July to December (October 2009 - June 2011) ...66
Figure 91 : control points for the statistics.....67
Figure 92 : Histograms of Hs for the 5 control points 67
Figure 93 : Hs monthly statistics for the 5 control points 68
Figure 94: Percentage of valid data per pixel.....69
Figure 95: Mask based on data availability. On the red pixels data availability is less than 50 %, therefore these data have been removed for subsequent analyses. 70
Figure 96: Mean Hs measured by the radars at Pendeen and Perranporth (March 2011 ï September 2012).....71
Figure 97: Maximum Hs measured by the radars at Pendeen and Perranporth (March 2011 ï September 2012).....71
Figure 98: Hs monthly means for months January to June. 72
Figure 99: Hs monthly means for months July to December. 73
Figure 100: Control points for the statistics.....74
Figure 101: Histograms of Hs for the 5 control points 74
Figure 102: Hs monthly statistics for the 5 control points. 75

1 Introduction

This report is a summarised translation of the technical report delivered in French by Actimar as an outcome of the study « Mesure, traitement et analyse des données de courants et dõétats de mer en mer dõIroise è conducted as part of the contract Ifremer/Actimar NÁ11/2 212 229 as well as original contributions from Plymouth University.

The study is divided in tasks described hereafter:

Task C1: Development of a new operational Direction Finding algorithm adapted to the WERA HF radars data.

Task C2: Comparison of the two methods ñDirection Findingò and ñBeam Formingò in the Fromveur area.

Task C3: Results validation by comparison of HF radars measurements with available in situ measurement.

Task C4: Surface current mapping over the Iroise sea and Fromveur area.

Task V1: Mapping of the statistics of the significant wave height (Hs) measured by HF Radars over the Iroise Sea, based on the empirical estimation method.

Task V2: Validation/Calibration of the empirical estimation algorithm by comparison with in situ measurement provided by a wave buoy.

Task V3: Comparison of the Hs estimated using two different methods: the empirical method and the Barrick's equation inversion.

2 Surface current measurement using WERA HF radars data

Actimar is exploiting under license of the Université Sud Toulon Var (USTV) the SORT2RADIAL software for the computation and mapping of surface currents from HF radar measurement using the Direction Finding (DF) method. The first objective of this study consists in developing a Direction Finding algorithm based on the one developed by USTV and adapted to the WERA HF Radars installed in the Iroise Sea area.

The results obtained using this DF method will be compared with the results obtained using the classical Beam forming (BF) method. Results will be validated using ADCP data sets collected during various surveys.

2.1 Development of the operational DF method for the WERA HF radars data

Current measurement processing using HF radars consist in selecting a target subarea at the surface of the sea and associate to this target or cell a radial current velocity. The distance of the target to the source is classically identified emitting chirps. The azimuth selection consists in assessing a relationship between the azimuth and the Doppler frequency associated with the target cell.

Two different approaches can be used for the azimuthal processing: either the Beam forming method or the goniometry, also called Direction Finding.

In the BF approach, the reception network is numerically oriented towards predefined azimuths. The Doppler frequency associated with the radial current is then estimated from the Doppler spectrum computed in each distance-azimuth cell.

In the DF approach, the process consists in first computing the Doppler frequency and then estimate the associated direction.

2.1.1 The SORT2RADIAL Processing tool

The DF method implemented in the SORT2RADIAL processing tool is based on the Multiple Signal Classification (MUSIC) algorithm in which the signal is modeled as the summation of a finite number of complex exponentials with random amplitudes and a white noise.

2.1.1.1 MUSIC Algorithm

The signal is modeled by the MUSIC algorithm as the summation of a finite number of complex exponentials with random amplitudes and a white noise. The observation space is split in two orthogonal sub-spaces: the signal space and the noise space. This decomposition is obtained by sorting in decreasing order the eigenvalues of the cross-spectral matrix.

If the number of complex exponentials is p, the p eigen vectors associated with the p highest values will create the space signal. A projection over the signal sub-space of a family of vectors parameterized by their direction of arrival it is possible to select only the vectors for which the projected norm constitutes a relative maximum This family of vectors is built assuming that the structure of antenna used for the detection of the arrival angles, that is the relative phase state of the signals on each sensor is known. Hence one of the main features of the MUSIC algorithm is that it can adapt to any structure of reception antennas network.

2.1.1.2 Azimuthal processing chain

The structure of the SORT2RADIAL programme is based on the MUSIC algorithm. The processing chain can be decomposed in successive tasks as presented on figure 2. After Doppler analysis, Doppler frequencies of interest and associated direction are processed independently by range ring.

Selection of these Doppler rays is obtained from the Doppler spectrum computed for the considered ring. For each selected ray, the cross-spectral matrix of the signal is estimated and the decomposition into eigen values and eigen vectors is made. Then the response of the network of antennas either measured or empirically estimated is projected on the signal space using the eigen vectors previously computed. The relative maxima of the projection function determine the directions associated with the considered Doppler ray. Finally, if more than one Doppler ray is found in the same range-azimuth cell, the one with the highest energy is conserved.

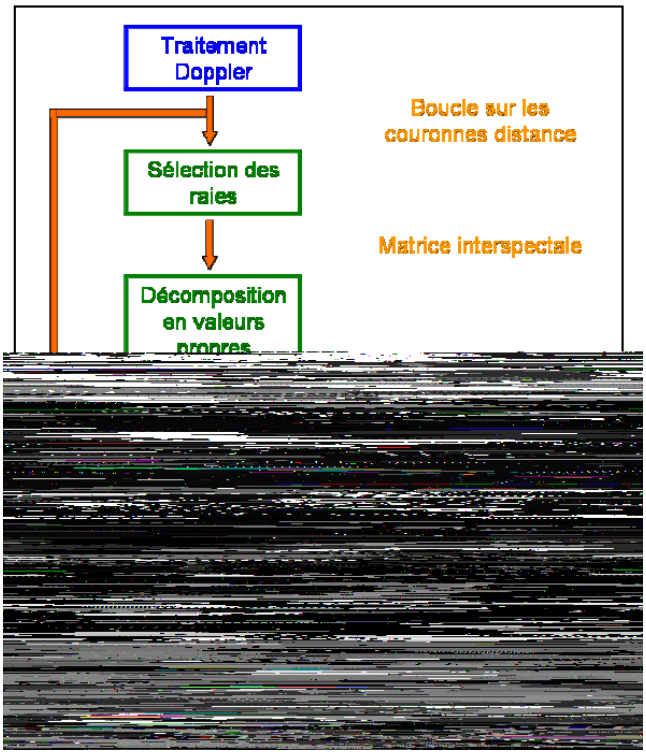

Figure 1 : SORT2RADIAL Azimuthal processing chain

2.2 Comparison of the two methods for the measurement of currents in the Fromveur area

A comparison of the two methods DF and BF of surface current measurement is first conducted over the Fromveur area (48.442044°N, -5.037099° W) (Figure 2).

Figure 2 : Fromveur area and reference measurement point (red dot).

Results are presented in the form of time series, scatter plots and Quantile-Quantile plots. Correlation coefficients and RMS values are also computed so as to compare the two methods.

2.2.2 North - South component

Presented here are results related to the North - South current vector.

Figure 5 : Time series for the 2 methods BF (blue) and DF (green), North - South component.

Correlation between two methods is 0.906211 and the RMS value is 0.323340 $m.s^{-1}$.

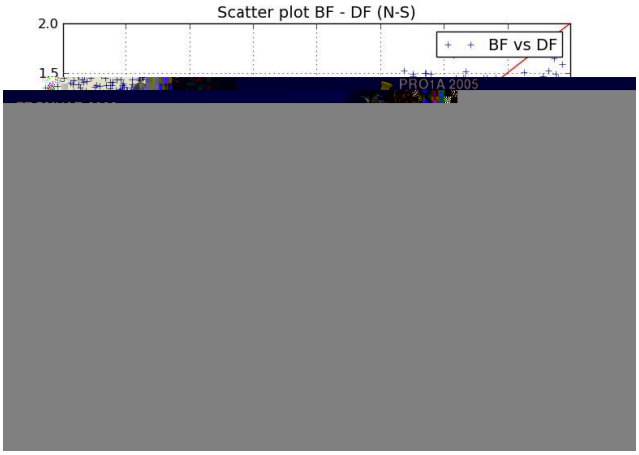

Figure 6 : Scatter plot and Q-Q plot for both methods BF and DF, North – South Component

The bounding effect visible at the extremes of the scatter plot and Q-Q plot is due to the definition of a maximal authorized radial velocity in the Direction finding method.

2.2.3 Norm of the total velocity vector

Presented here are results related to the norm of the total vector of the measured current.

Figure 23 : Scatter plot and Q-Q plot for both methods BF (blue) and DF (green) as functions of ADCP measurement, North - South Component

ref ADCP BeGhO1nTJ 9 9C>21 0 0 1 140.9 443. Tm7ot77[C>21 0 70TJ tuBen9.0.621 0 0 1 140.9 443. Tm7ot0

Data used in this chapter are surface currents measured by WERA HF radars owned by SHOM and located at Garchine and Brézellec and processed using the Beam forming methods, for the period July 2006 ï August 2011.

2.4.1 Statistics of the space distribution of measured surface currents

Figure 28 presents the area covered by the HF radars and the rate of coverage over the whole period (July 2006 ï August 2011). The area having a rate of coverage larger than 50% is used for the assessment of the statistic indicators.

Mean current velocity amplitude over the July 2006 ï August 2011 period are presented figure 29. Mean current velocity is higher than 0.4 m/s over almost the whole area. It is 0.8 m/s in the Fromveur and over 1 m/s in the north-west of Ushant Island.

Median value of surface currents, that is the velocity amplitude reached 50% of the time, is shown figure 30. 99% quantiles of measured surface currents are given figure 31. Measured velocities are higher than 2 m/s around Ushant and up to 3 to 3.5 m/s in the north-west of the island.

Rates of occurrence of current velocities above 0.25, 0.5, 0.75, 1 and 1.5 m/s thresholds are presented Figures 32 to 36. Measured velocities are higher than 0.25 m/s more than 50% of the time over the whole considered area. Velocities are higher than 0.5 m/s over 70% of the time in the Fromveur and in the north-west of Ushant Island. They are above 1 M/s at least 30% of the time in the Fromveur and 50% of the time in the north-west of the island.

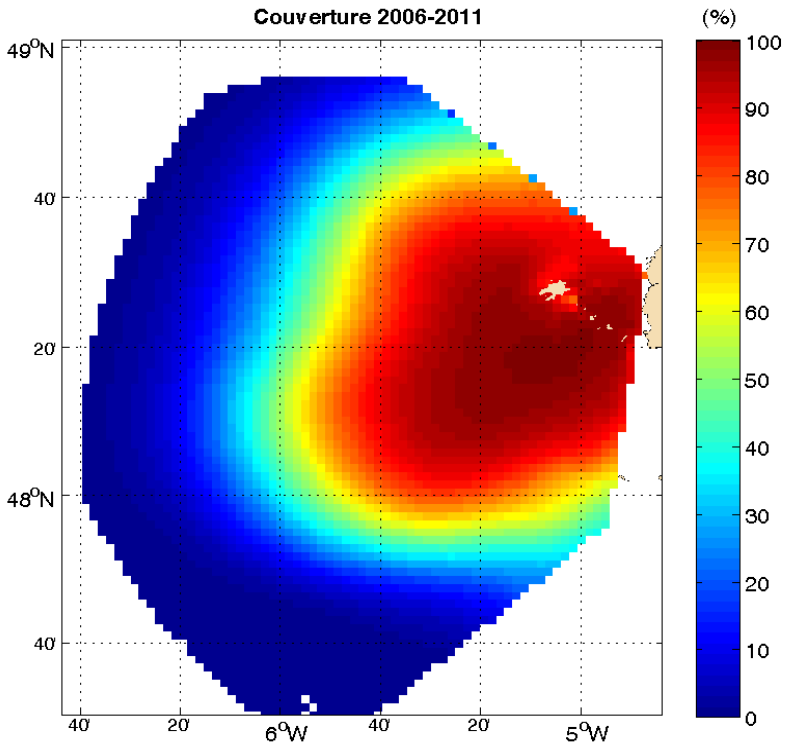

Figure 28 : space coverage and rate of occurrence of surface current measurement over the period 07/2006 - 08/2011

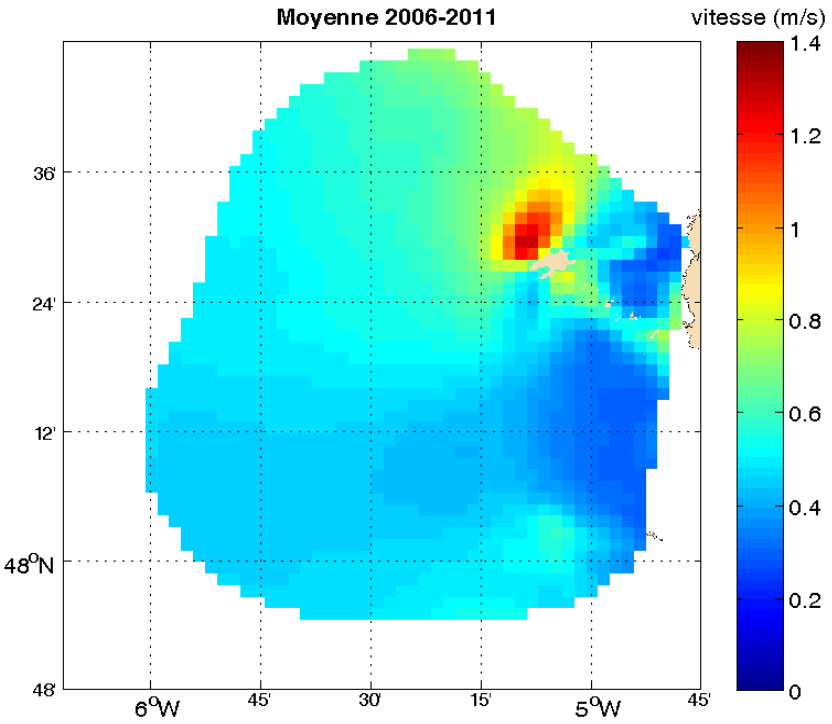

Figure 29 : mean surface current velocity amplitudes over the period 07/2006 - 08/2011

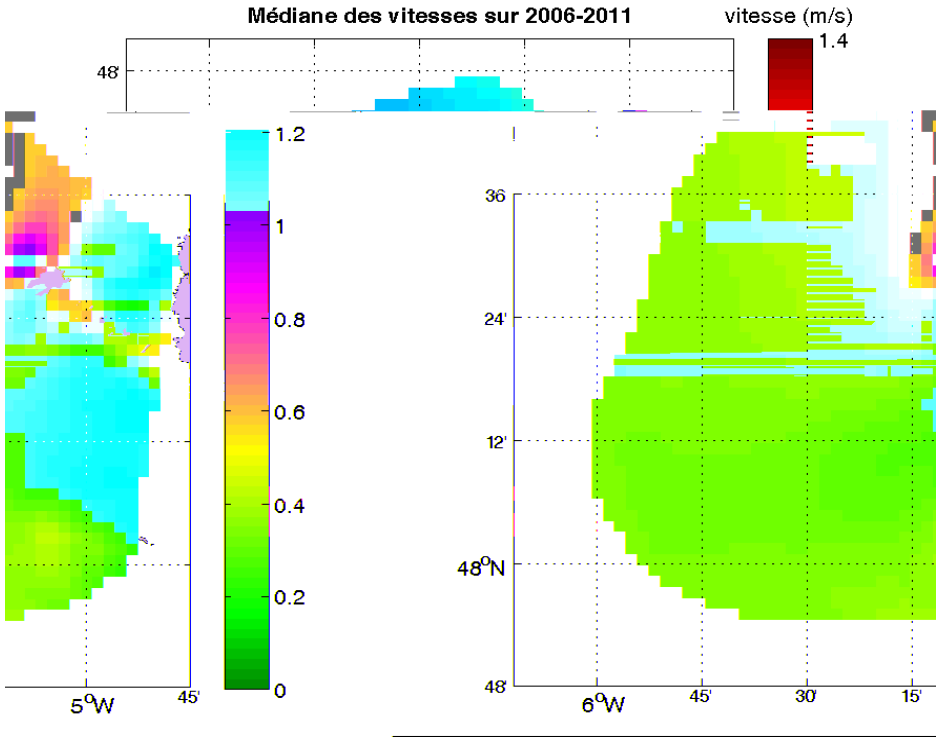

Figure 30 : Median value of surface current velocity amplitudes over the period 07/2006 - 08/2011

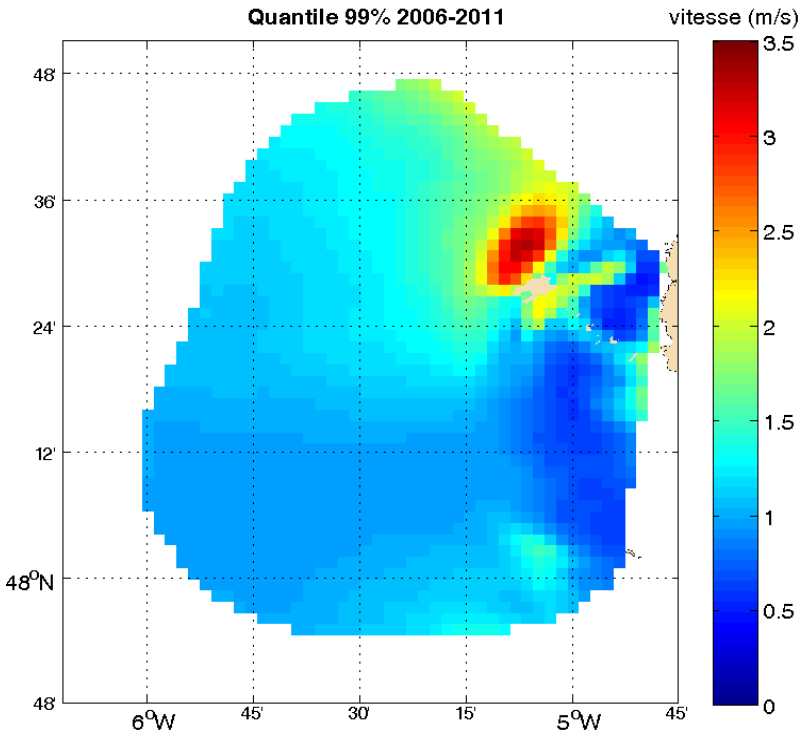

Figure 31 : 99% quantile of surface current velocity amplitudes over the period 07/2006 - 08/2011

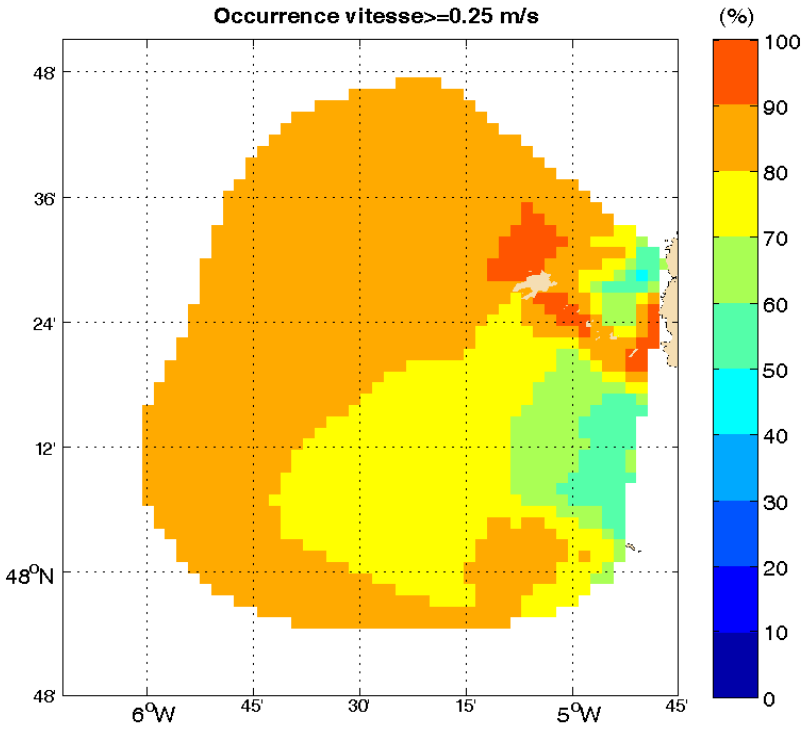

Figure 32 : Probability of occurrence of velocities higher than 0.25 m/s over the period 07/2006 - 08/2011

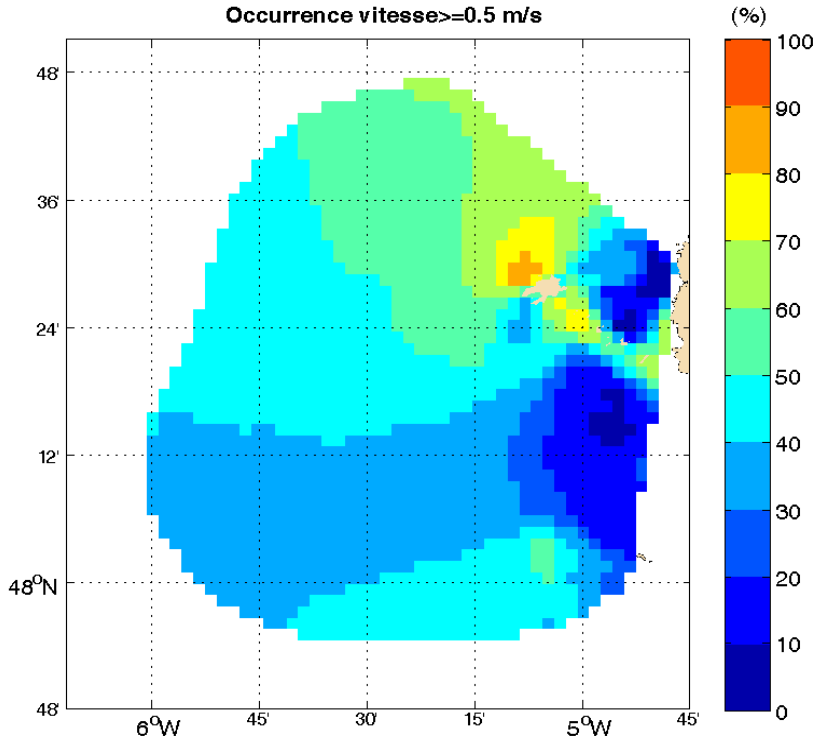

Figure 33 : Probability of occurrence of velocities higher than 0.5 m/s over the period 07/2006 - 08/2011

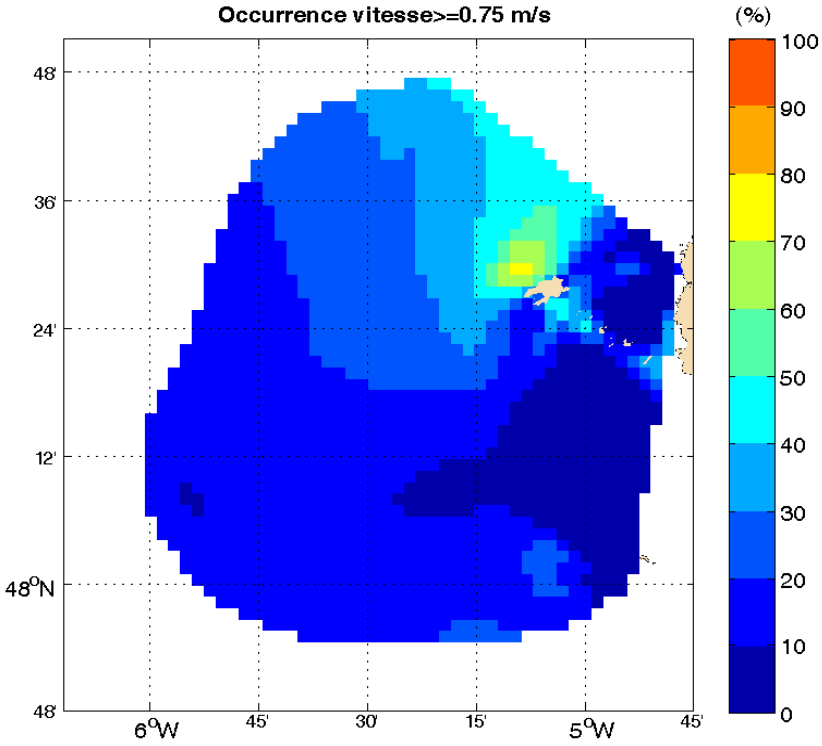

Figure 34 : Probability of occurrence of velocities higher than 0.75 m/s over the period 07/2006 - 08/2011

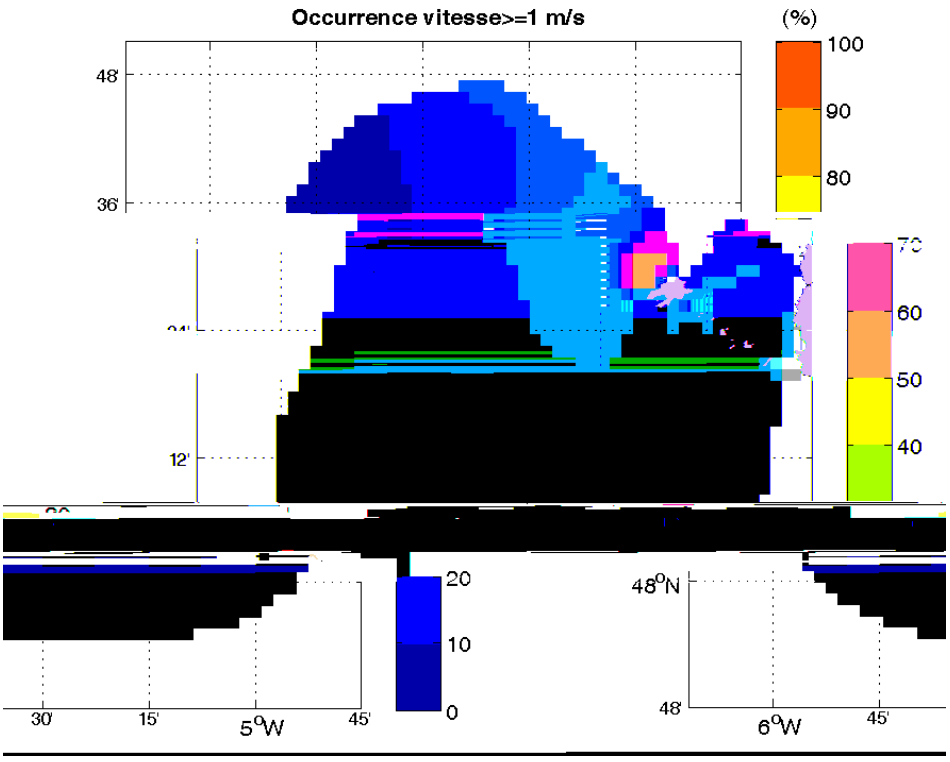

Figure 35 : Probability of occurrence of velocities higher than 1 m/s over the period 07/2006 - 08/2011

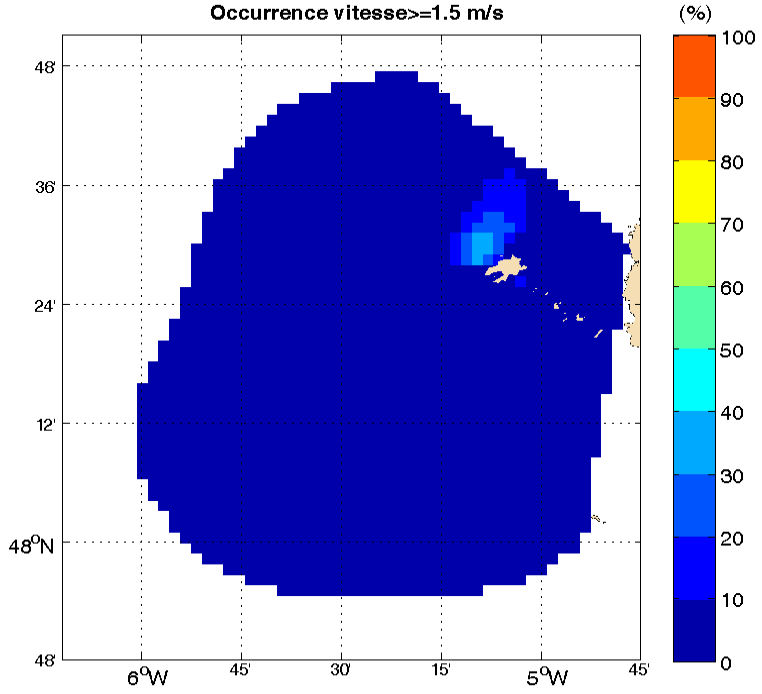

Figure 36 : Probability of occurrence of velocities higher than 1.5 m/s over the period 07/2006 - 08/2011

2.4.2 Space distribution statistics of currents direction

Frequency of occurrence of surface currents directions are presented figure 37 in the form of polar histograms superimposed to the map of the average velocity amplitudes.

Same kind of histograms are presented figure 38 in the limited area around Ushant island and compass roses corresponding to the 16 points marked on the figure are presented figure 39.

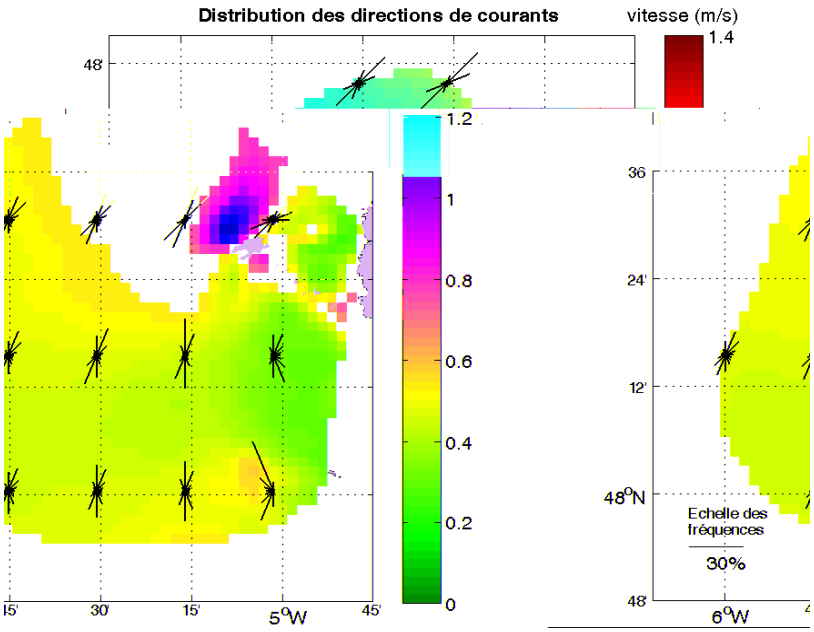

Figure 37 : Frequency of occurrence of directions (polar histograms) superimposed with mean velocity amplitude of surface currents over 07/2006 - 08/2011

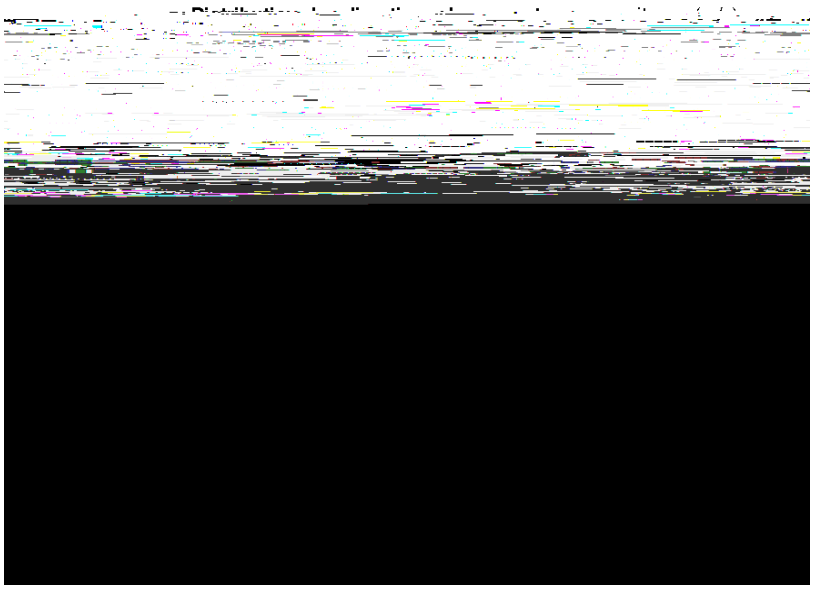

Figure 38 : Frequency of occurrence of directions (polar histograms) superimposed with mean velocity amplitude of surface currents around Ushant Island over 07/2006 - 08/2011

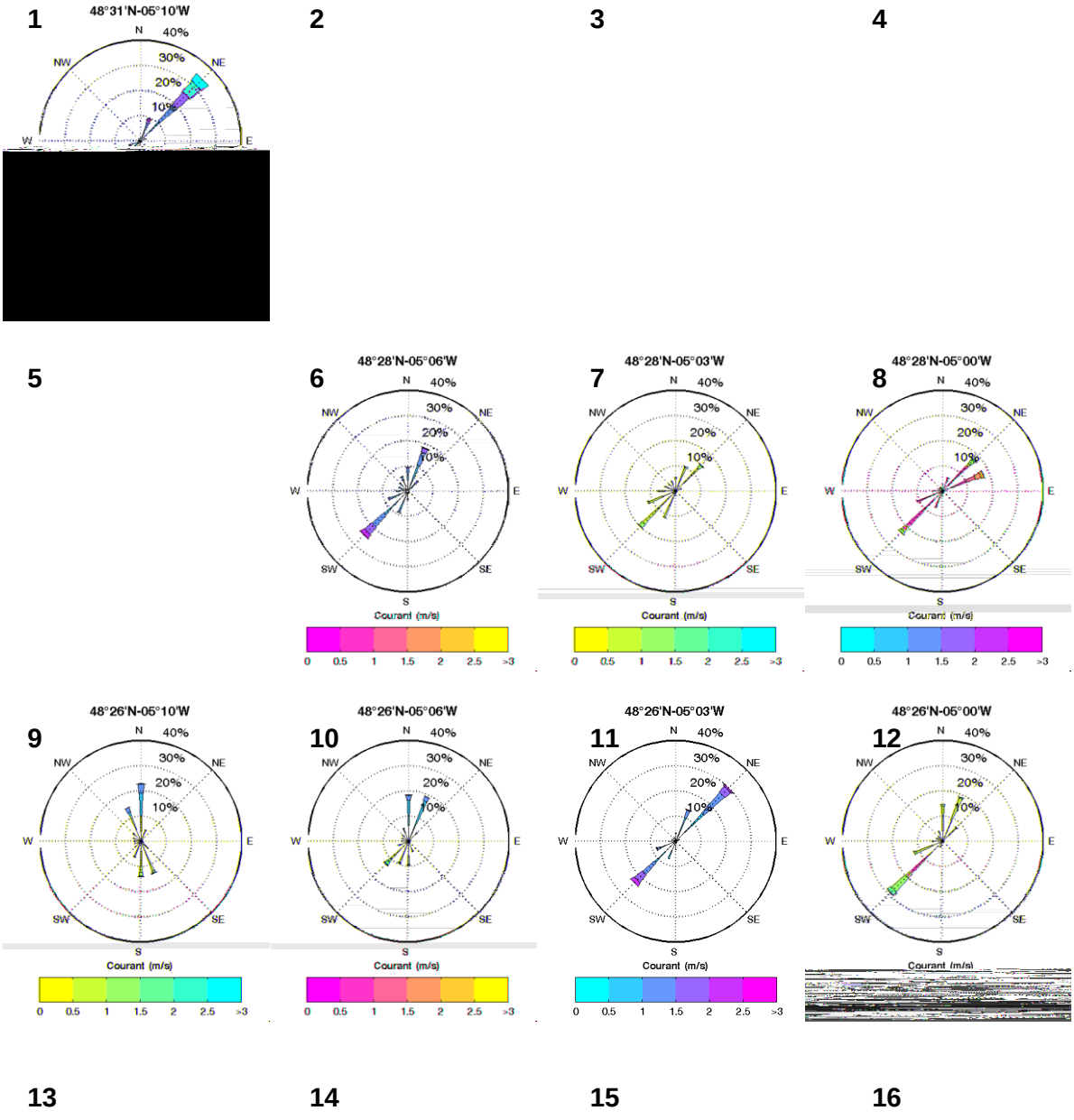

Figure 39 : Surface currents compass rose around Ushant Island, 07/2006 - 08/2011

2.4.3 Scientific analysis around Ushant Island

Global statistics for surface currents at the point N° 11 located in the Fromveur strait, including velocities and direction histograms, a compass rose for the whole data set and a compass rose for currents higher than 0.5 m/s are presented figure 40.

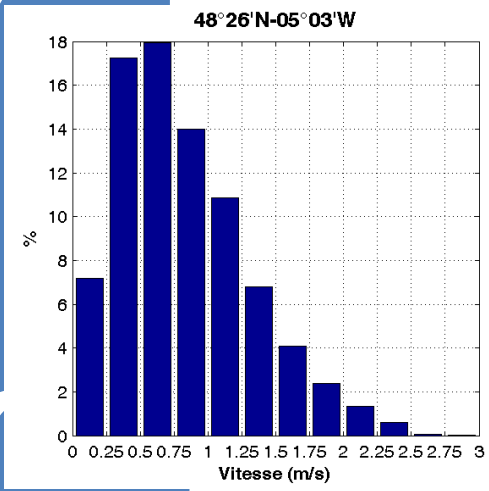

m (upper left), directions histogram (upper right), currents compass rose (lower left), se for currents > 0.5 m/s (lower right).

Global statistics for surface currents at the point N° 5 located in the north-west of Ushant island, including velocities and direction histograms, a compass rose for the whole data set and a compass rose for currents higher than 0.5 m/s are presented figure 41.

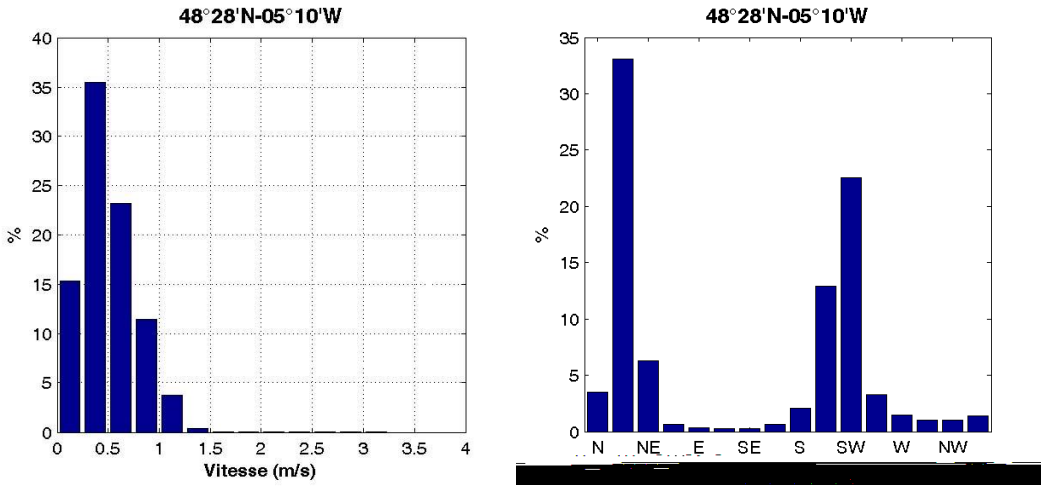

Figure 41 : Statistics in the North-west of Ushant island (Point N°5) over the period 07/2006 - 08/2011. Velocity amplitudes histogram (upper left), directions histogram (upper right), currents compass rose (lower left), currents compass rose for currents > 0.5 m/s (lower right).

2.4.4 Tides analysis

2.4.4.1 Methodology

Currents compass roses are assessed for several points of the radar grid for different values of tidal coefficients : 45, 70 and 95. Currents compasses are assessed from 6 hours before high tide (PM-6) to 6 hours after high tide (PM+6) considering Brest harbor as the reference. Therefore, 10 events (12 h period around high tide time in Brest) of each tidal coefficient. The current associated with each coefficient is then computed as the average value of the observed currents for the 10 considered events.

As an example, Intensity and direction of currents measured for various events corresponding to a tidal coefficient of 45 at the point 4.9981°W, -48.4027° N between PM-6 and PM+6 are presented figure 42. This shows that flood is oriented towards North-North-

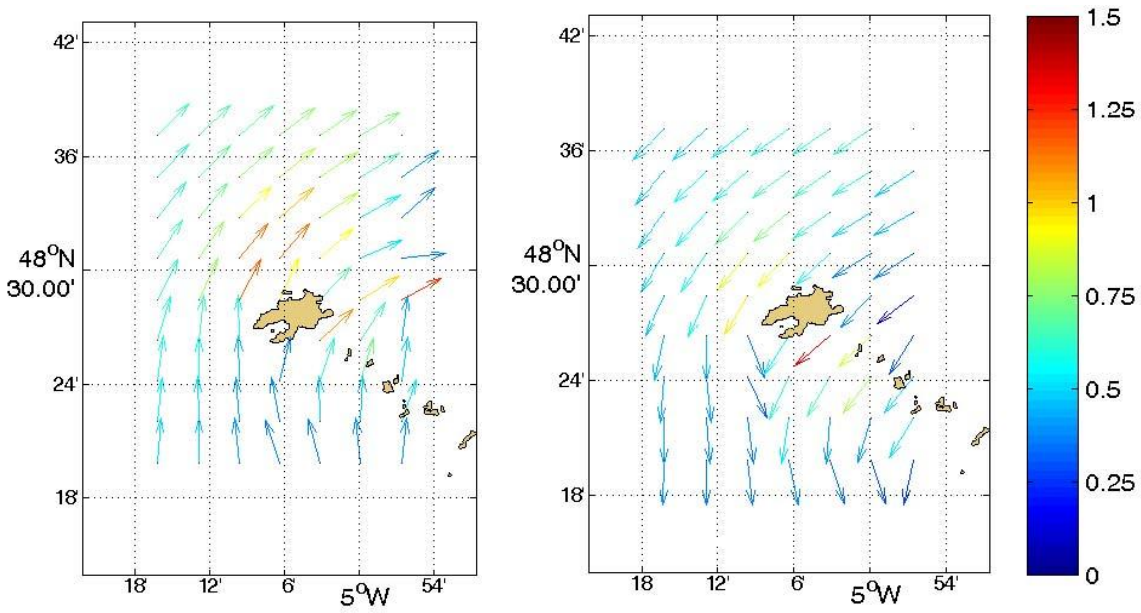

Figure 46 : Max of current velocity amplitude for flood (left) and ebb (right) for a tidal coefficient of 45

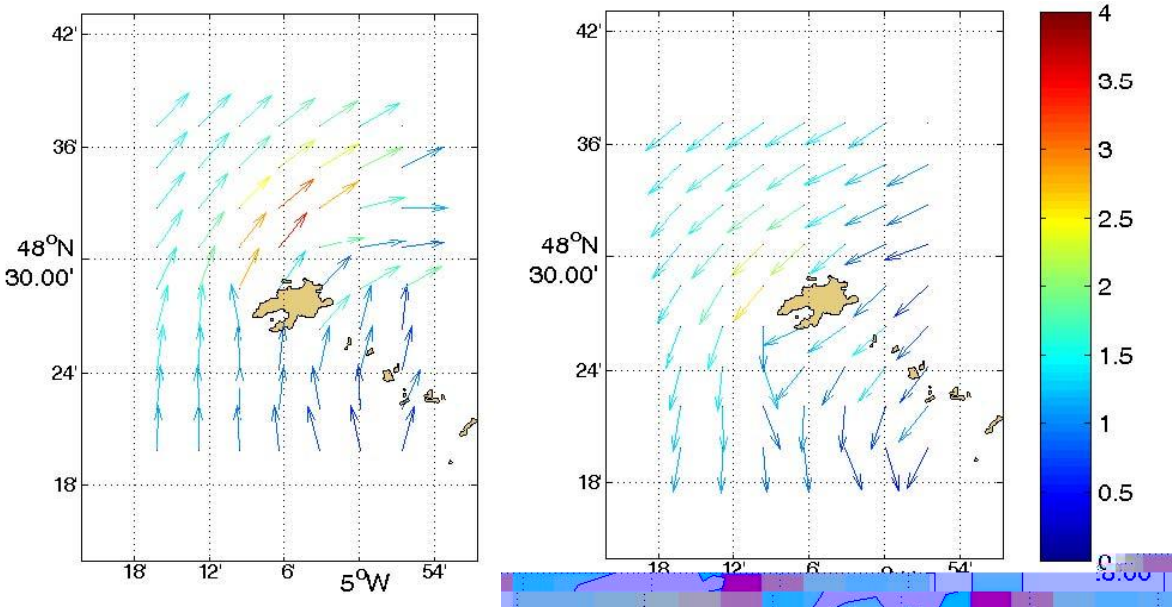

Figure 47 : Max of current velocity amplitude for flood (left) and ebb (right) for a tidal coefficient of 95

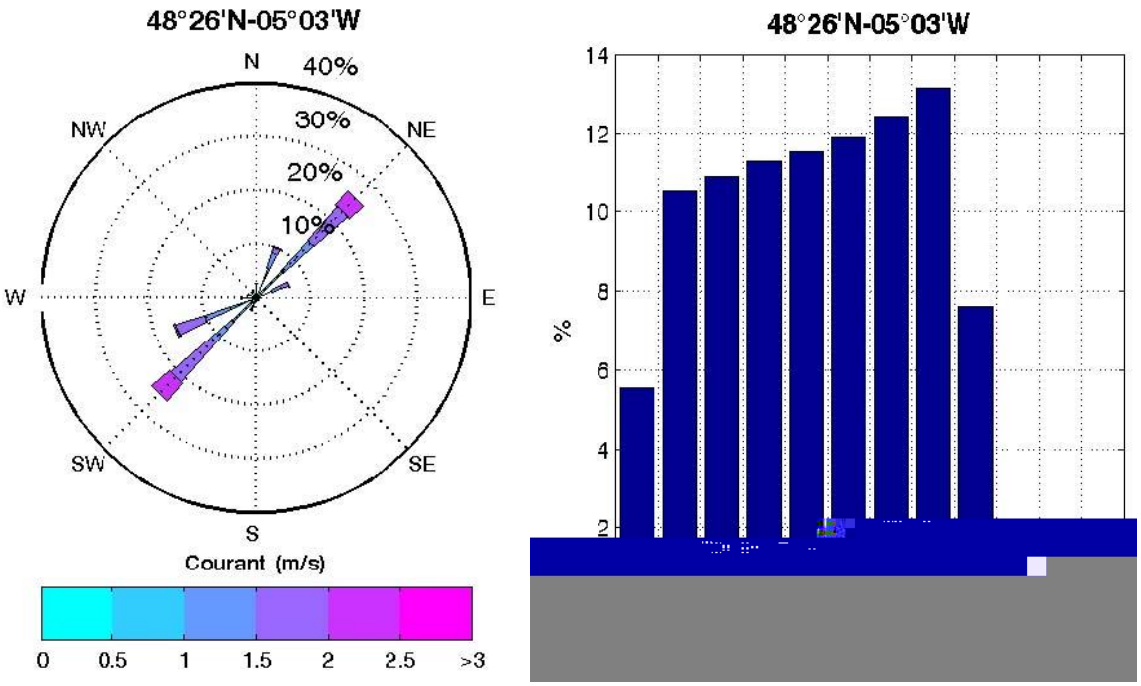

Figure 50 : DF method, statistics in the Fromveur strait (point N°11) : velocity compass and histogram.

3 Sea-states measurement from WERA HF radars: processing and analysis

3.1 Significant wave height (Hs) measurement using WERA HF radars

3.1.1 Classical empirical method

3.1.1.1 Description

Analysis of WERA HF radar measurement allows significant wave height assessment. In the first part of this study, the Hs parameter is obtained from HF radar data using the empirical algorithm developed by K. W. Gurgel[1] . This algorithm links the normalized spectral energy density of the radar second order Doppler spectrum to the wave energy spectral density by mean of empirically estimated coefficients. The significant wave height Hs is then computed by summation of the estimated omnidirectional wave spectrum. The empirical coefficients used here to produce the Hs from HF radar data over the period from 2009 to 2011 were determined by K. W. Gurgel from the data set recorded in Norway during the European Radar Ocean Sensing (ñEuroROSEò) project (Sept 1998-Oct. 2001).

3.1.1.2 Quality control of radars measurement

Comparisons of Hs measured by radar with Hs measured by wave buoys (CANDHIS data sets) were performed so as to assess the quality of radar measurements.

Time series of the significant wave height measured by radars were extracted at the locations of the wave buoys (Figure 51).

- Datawell wave buoy 02911 ï Les Pierres Noires ï 48Á17.42ôN, -04Á58.10ôW, water depth 60 m. Hourly Hs data is available until July 26th 2010 (data provided by SHOM).
- Buoy 02902 ï Ouessant large 48Á30ôN, -05Á45ôW, water depth 110 m. Hourly Hs data is available over the whole period 2009 ï 2011.

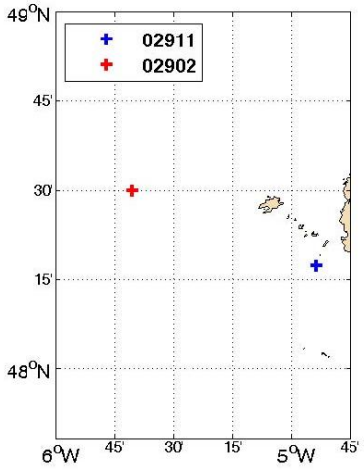

Figure 51 : Location of wave buoys used for the analysis

[1] K.-. GURGEL, H.H. ESSEN and T. SCHLICK, 2006. An empirical method to derive ocean waves from second order Bragg scattering ï Prospects and limitations. IEEE Journal of Oceanic Engineering,

The HF radar data is available with a 30 minutes time step. For this comparison the HF radar data are compared with the data corresponding to the closest date in the wave buoy time series.

Time series, scatter plots and Quantiles-Quantiles plots are presented Figure 52 for buoy 02911 and Figure 53 for buoy 02902.

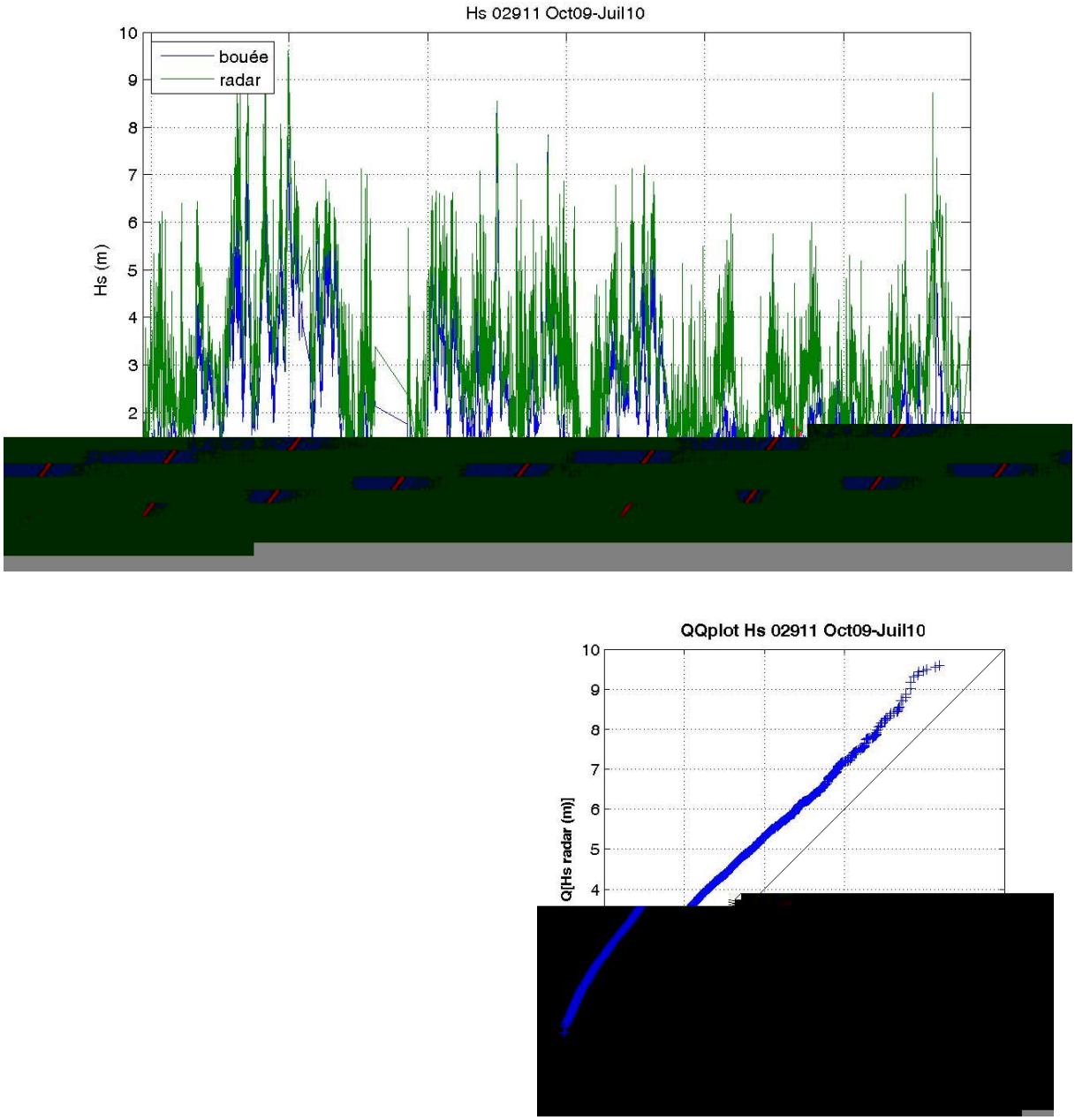

Figure 52 : comparison of HF radar and 02911 wave buoy Hs data - October 2009 to July 2010.

Figure 53 :

eliminating possible erroneous measurements provided by the radars. This choice also implies a more strict selection of the input data and, as a consequence a slightly lower number of output data. Additionally, it requires a specific calibration of the integration coefficients.

3.1.2.2 Quality control of the radar measurements

In order to assess the quality of the measurement obtained using the modified empirical method, time series of Hs measured by HF radars and wave buoys are compared.

Time series of the significant wave height measured by radars were extracted at the locations of the wave buoys using the same buoys data sets as in the previous section.

Time series, scatter plots and Quantiles-Quantiles plots are presented Figure 57 for buoy 02911 and Figure 58 for buoy 02902.

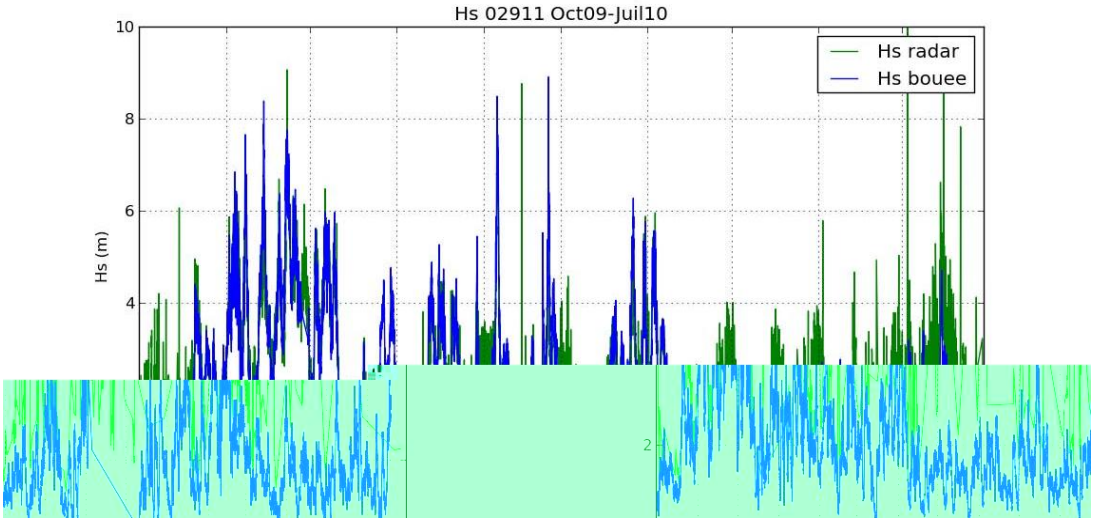

Figure 57 : comparison of HF radar and 02911 wave buoy Hs data - October 2009 to July 2010 - Modified empirical method

3.1.2.3 *Discussions on the results of the modified empirical method*

We discuss in this chapter the results obtained when using the modified empirical method.

We consider at first the time series of the significant wave height at the location of the buoy 02911 for the month of December 2009.

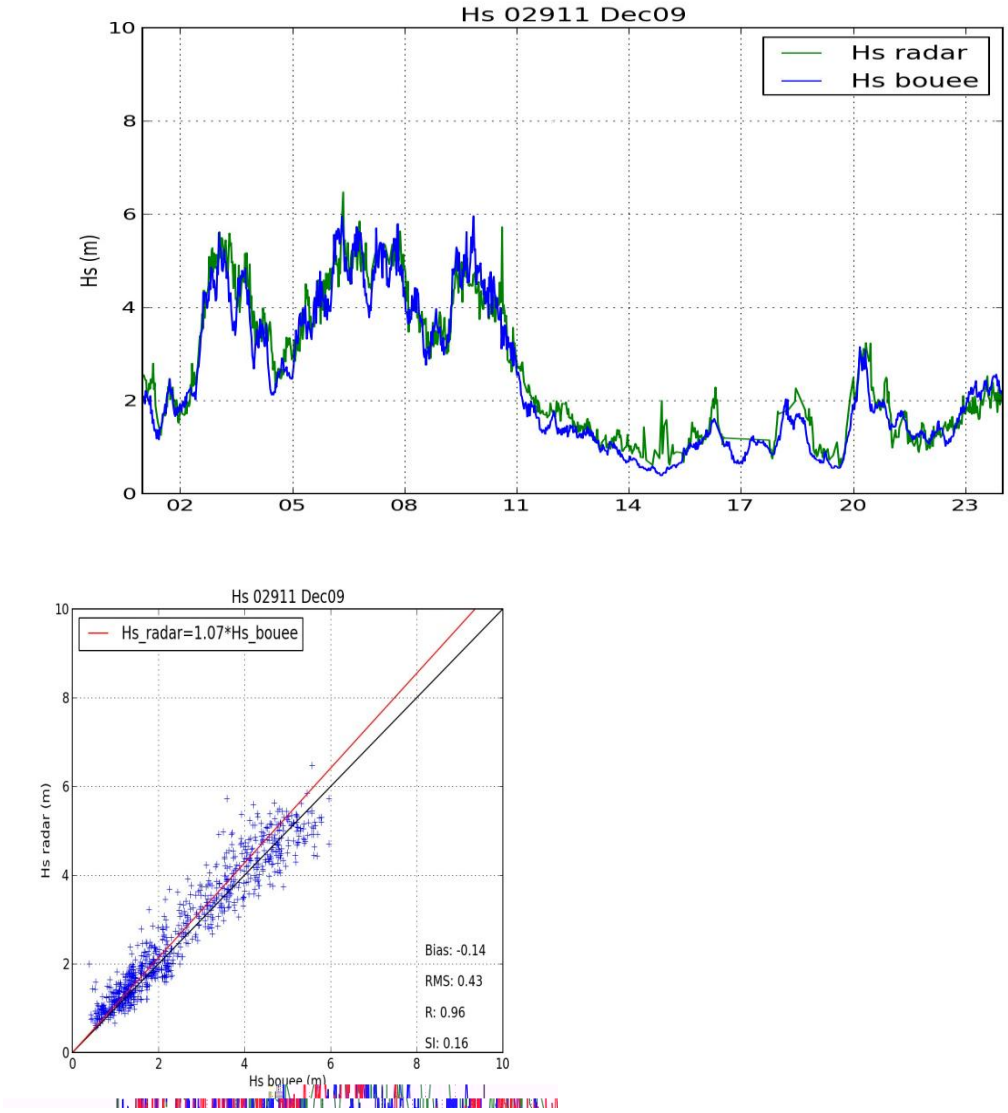

Figure 59 : Comparison of Hs measured by the wave buoy 02911 and estimated from radar data using the modified empirical method - December 2009

These results confirm that the modification of the empirical method for an adaptation to the specific configuration of the radars in the Iroise Sea area yields a significant improvement of the quality of the Hs radar measurement at the location of the buoy 02911 ñ Les Pierres Noiresò

In order to explain the results observed at the buoy 02902 ñOuessant largeò, a comparison is made with the significant wave height data obtained from a numerical model (WWIII Norgas hindcast database).

Comparison of the buoy data with the model data is presented figure 60 and shows that in spite of a good correlation (0.96) between in-situ measurement and model, the bias is 50 cm

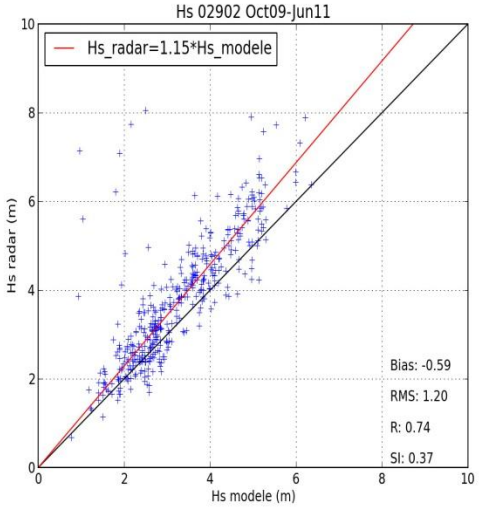

Figure 63 : Norgas model significant wave height compared with radar measurements using the modified empirical method at the location "Ouessant Large".

3.1.2.4 Testing of modified algorithms on the Plymouth University data sets

Plymouth University (PU) is operating two WERA HF radars along the coast of Cornwall. The radars are located at:

- Perranporth 50Á20.06ôN, -05Á01.56ôW
- Pendeen 50°09.80ôN, -05Á39.98ôW

Data acquisition and processing are similar to those of the radars located in the Iroise Sea so that the procedures developed for the Iroise Sea radars can also be applied to the PU data sets with only minor modifications to the algorithms.

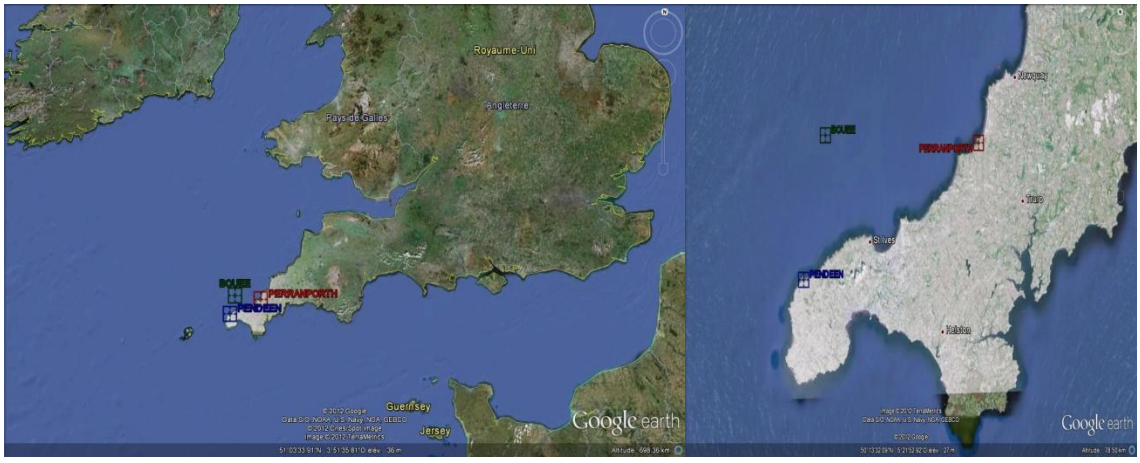

Figure 64 : Location of the PU HF radars and reference wave buoy

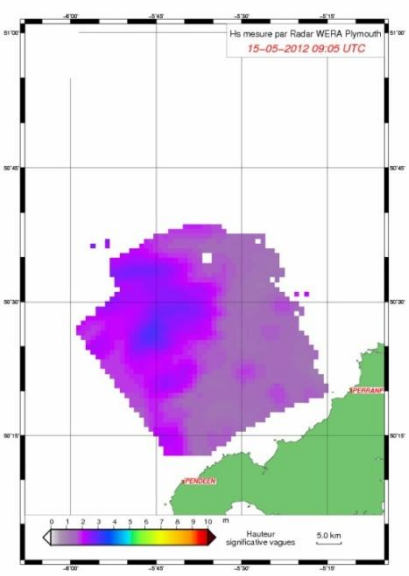

Figure 65 : Map of Significant wave height measured by the PU HF radars

The significant wave height assessed using the classical and modified empirical methods are compared to in-situ measurements using data provided by the wave buoy with coordinates 50Á20.5ôN, -05Á36.5ôW, over the month of May 2012.

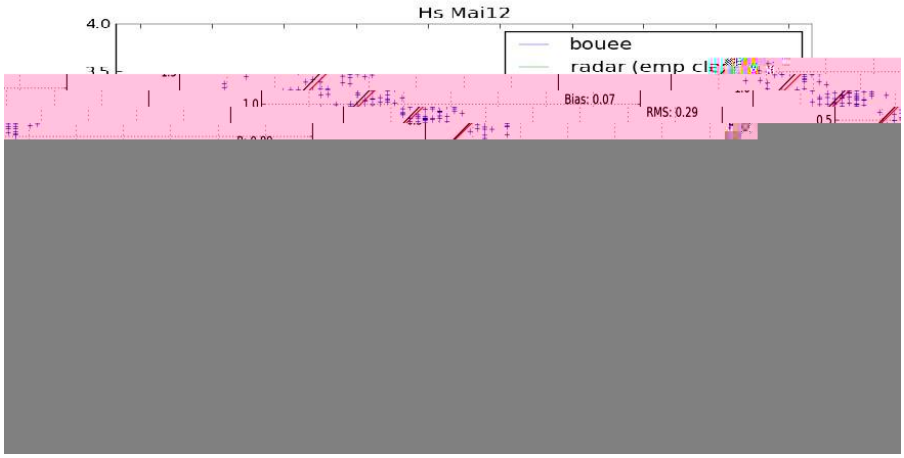

Figure 66 : Comparison of the classical (left) and modified (right) empirical methods with wave buoy data - PU radar data

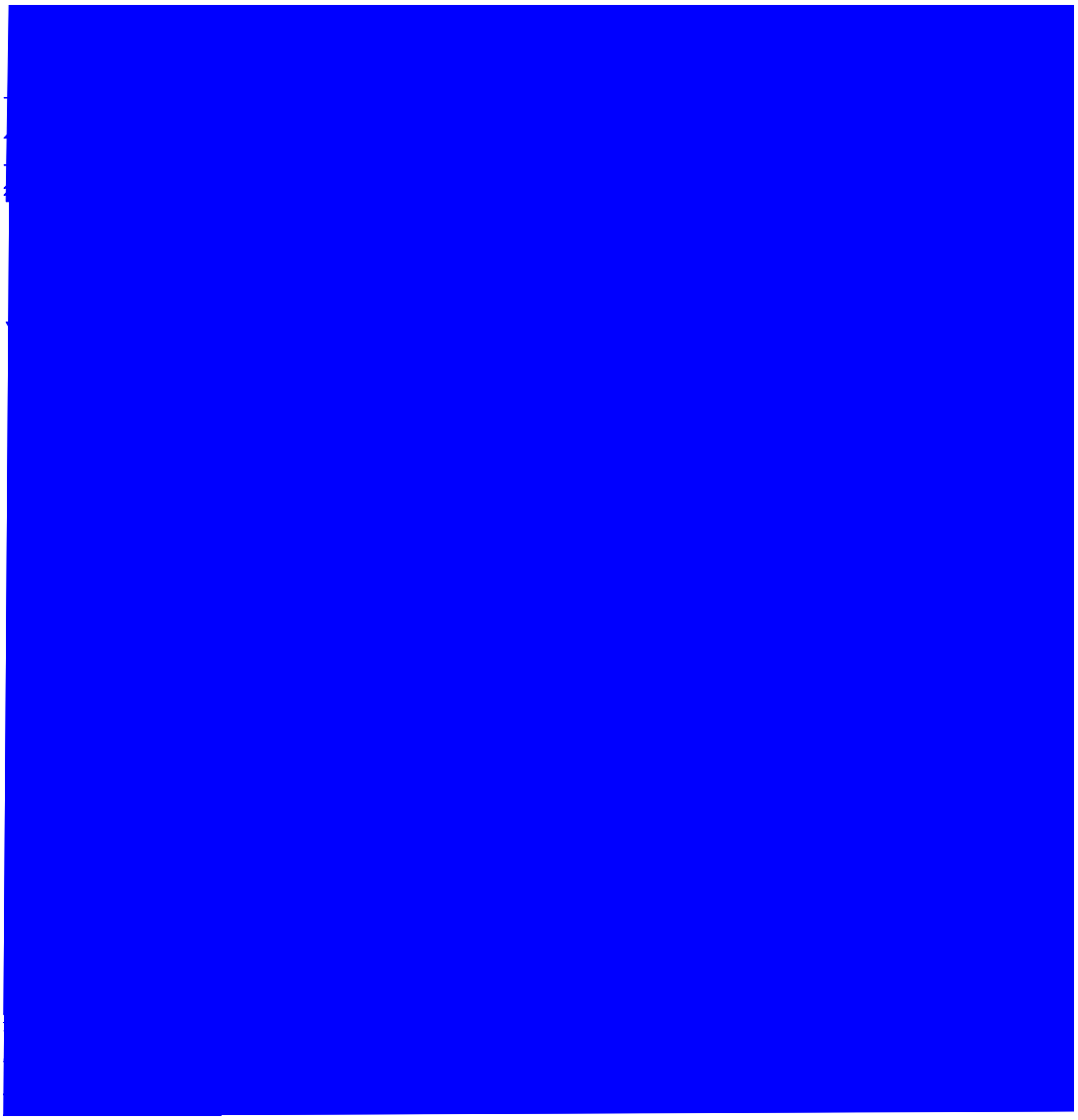

Figure 69: Comparison between radar Hs and Wave Hub buoy before calibration – March 2012 to December 2012.

The results obtained with the algorithm before calibration show good correlation between the wave buoy and the radar wave heights. As opposed to the Iroise Sea the bias is small (< 0.02 m) and both the buoy and the radar distributions are similar.

In spite of the better agreement between buoy and radar wave heights and the lack of many large spikes on the Celtic Sea radar dataset as compared to the Iroise sea case, the algorithm has been calibrated with measurements collected *in-situ* following the procedure described in the previous section in order to see if there is an improvement. The results after this calibration are depicted in Figure 70.

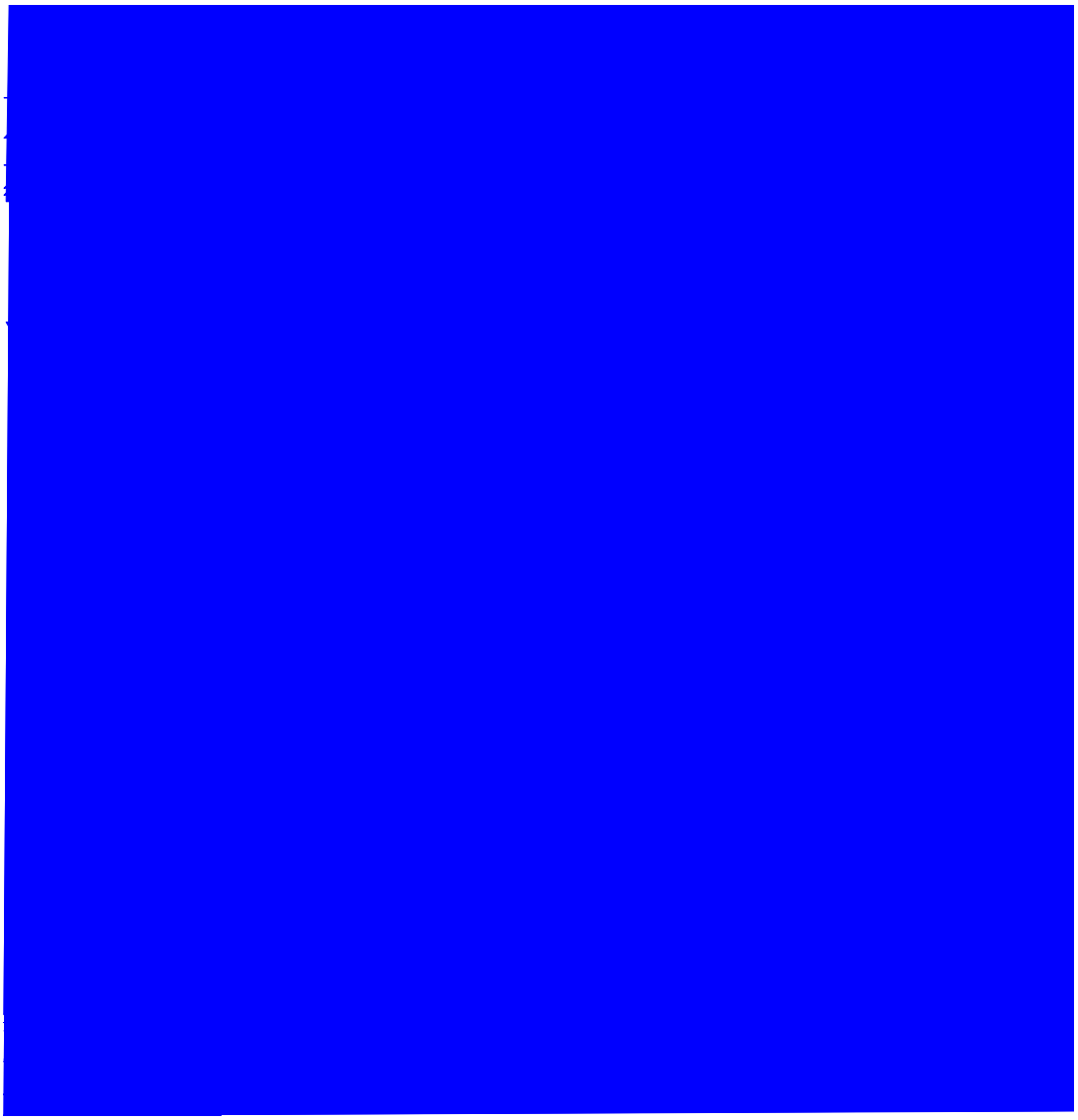

Figure 70: Comparison between radar Hs and Wave Hub buoy after calibration – March 2012 to December 2012.

The Q-Q plot in Figures 69 and 70 shows that the most noticeable effect of applying a calibration is better agreement of the buoy and radar distributions in the tail of highest values of Hs. The measured statistical indicators show a reduction in the scatter index of 0.01, a 1% increase in correlation, and a 2.8% error reduction for the period assessed.

3.1.3.3 Discussion on the results of the modified empirical method

In addition to the previous figures, a comparison between Hs measured by the wave buoy and radar estimates, obtained with the modified empirical method over May 2012, is shown in Figure 71. The purpose of this figure is to provide a reference for comparison to the results obtained for the same dataset, but by applying both the calibrated method adapted for the Iroise Sea and the non-calibrated algorithm (Figure 66).

Doppler spectrum measured by the HF radar, the information that is relevant for the characterization of waves is part of the second order so that the directional wave spectra can be estimated using inversion methods for the equations describing the second order. The equation describing the second-order backscattering coefficient is non-linear relative to the wave directional spectrum. Hence two different approaches are available:

- Linearize the second-order equation and solve the linear system
- Solve the non-linear equation

The linearized approach is the one adopted by L. R. Wyatt[3] and implemented in the commercial software SeaView. This method is also used for processing the HF radar data from the Iroise Sea.

The only existing method for the assessment of the wave directional spectrum without linearization of the equation describing the second order is the one proposed by Y. Hisaki[4].

This method consists of computing the second order equation for the HF radar configuration. Therefore, the directional wave spectrum is discretized, the points of the directional spectrum necessary for the assessment of the energy of the backscattered signal are saved and a non-linear inversion method such as Gauss-Newton or Marquart is finally used. As this nonlinear problem is ill-conditioned, it is necessary to impose constraints to the solution.

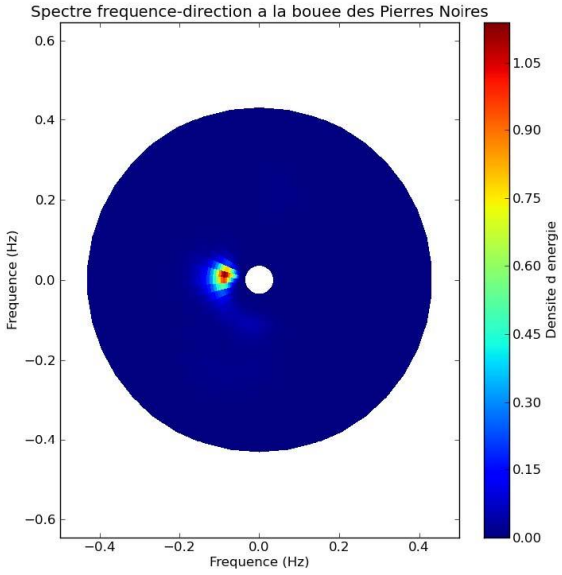

Figure 72 : Wave directional spectrum obtained from nonlinear inversion of the radar data - "Pierres Noires " location - January 15th 2010 midnight

[3] J.J. Green, discretizing Barrick's equations, Proceedings of Wind over Waves II: Forecasting and fundamentals of applications, 219-232, 2003
J.J. Green and L.R. Wyatt, Row action inversion of the Barrick-Webber equations, J. Atmos. Oceanic. Technol., 23, 501-510, 2006.

[4] Y. Hisaki, Nonlinear inversion of the integral equation to estimate ocean wave spectra from HF radar, Radio science, 31, 25-39, 1996.

3.1.4.2 *Nonlinear inversion based on Hisaki formulation*

The nonlinear inversion method for the Barrick equation based on Hisaki formulation was implemented and used for the processing of the Iroise Sea HF radar data. Various wave parameters can be derived from the directional spectrum. For instance, from the spectrum assessed at the location ñLes Pierres Noiresò on January 15th 2010 at midnight (Figure 67), the derived Hs is 2.51 m, the peak period is 11.6 s and the peak direction is about 270°.

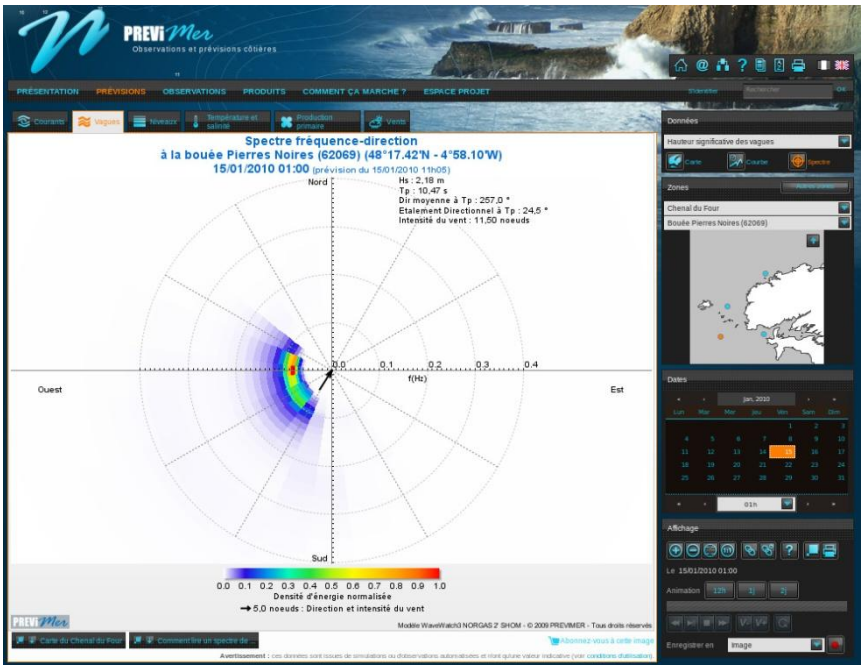

Figure 73 : Wave directional spectrum obtained WWIII Norgas wave model - "Pierres Noires " location - January 15th 2010 midnight

For validation purpose, these results are compared with the parameters obtained from the WWIII Norgas wave model at the same location and same date. Values provided by the model are Hs = 2.18 m, peak period 11.47 s, and peak direction 260° (Figure 68).

Results of numerous applications of this inversion procedure confirm that it is possible to assess the wave directional spectrum and the derived parameters using a non-linear inversion method. However, these results also confirm that this is not an easy problem to solve. The estimation of the wave directional spectrum from the Doppler spectrum is an ill-conditioned non-linear problem. The solution obtained after inversion also depends on the model initially used and several wave directional spectra can be obtained from one single input data set. The problem is depicted in Figures 69 and 70 : from two different initial directional spectra, the inversion algorithm converges towards two different directional spectra which describe in a similar way the input data but with a different physical meaning.

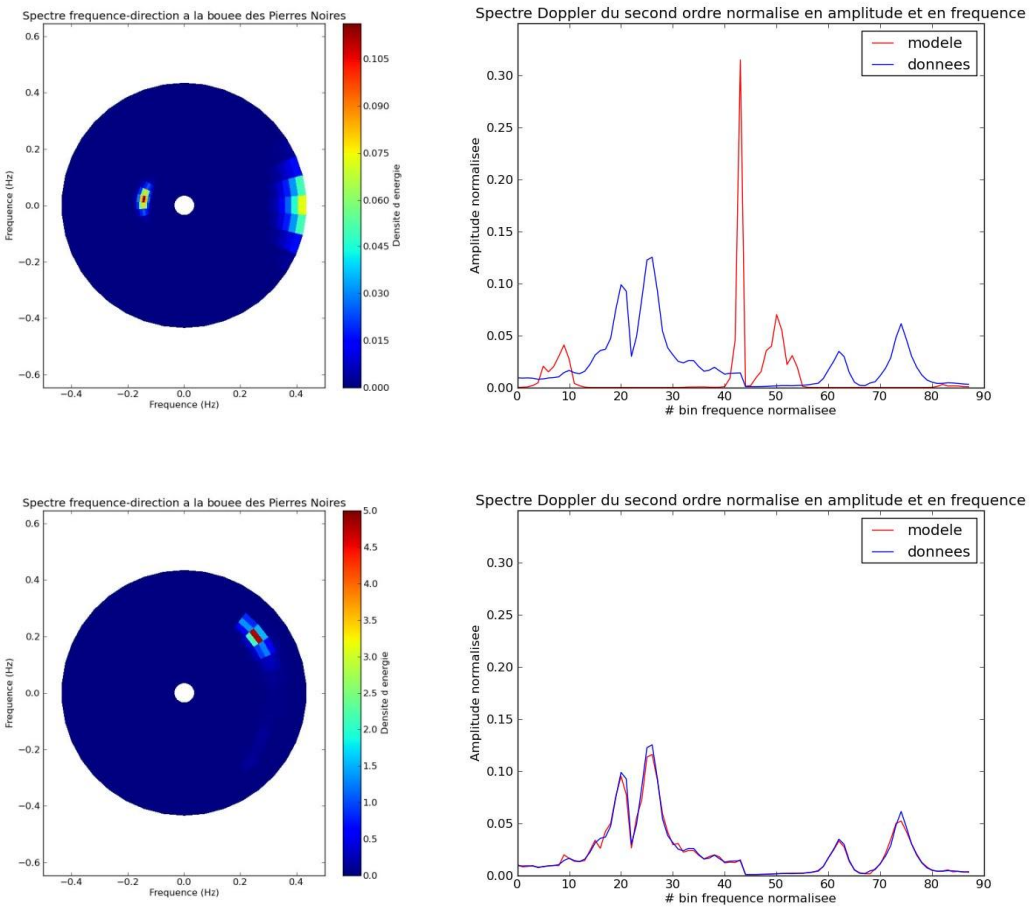

Figure 74 : Wave spectra and second order Doppler spectra on October 14th 2009 03:00 - "Les Pierres nNoires". Initial model (upper plot), final model after inversion (lower plot)

So far, the non-linear inversion algorithm based on Hisaki formulation is providing good results from a mathematical or theoretical point of view but all results do not necessarily have a correct physical meaning. It can be envisaged for improvement of the quality of the inversion process to add information, whether it is a priori (for instance in the Iroise Sea there is often westerly swell) or a constraint like, for instance, wind intensity and direction.

3.1.4.3 Comparison of the linearized and empirical methods

As the results obtained using the non-linear inversion method are not quite satisfactory, we focus here on the comparison of results using the linearized inversion method (SeaView) and the modified empirical method presented in the previous chapters. This comparison is made using data assessed at the ñPierres Noiresò location over the period October 2009 ï December 2009.

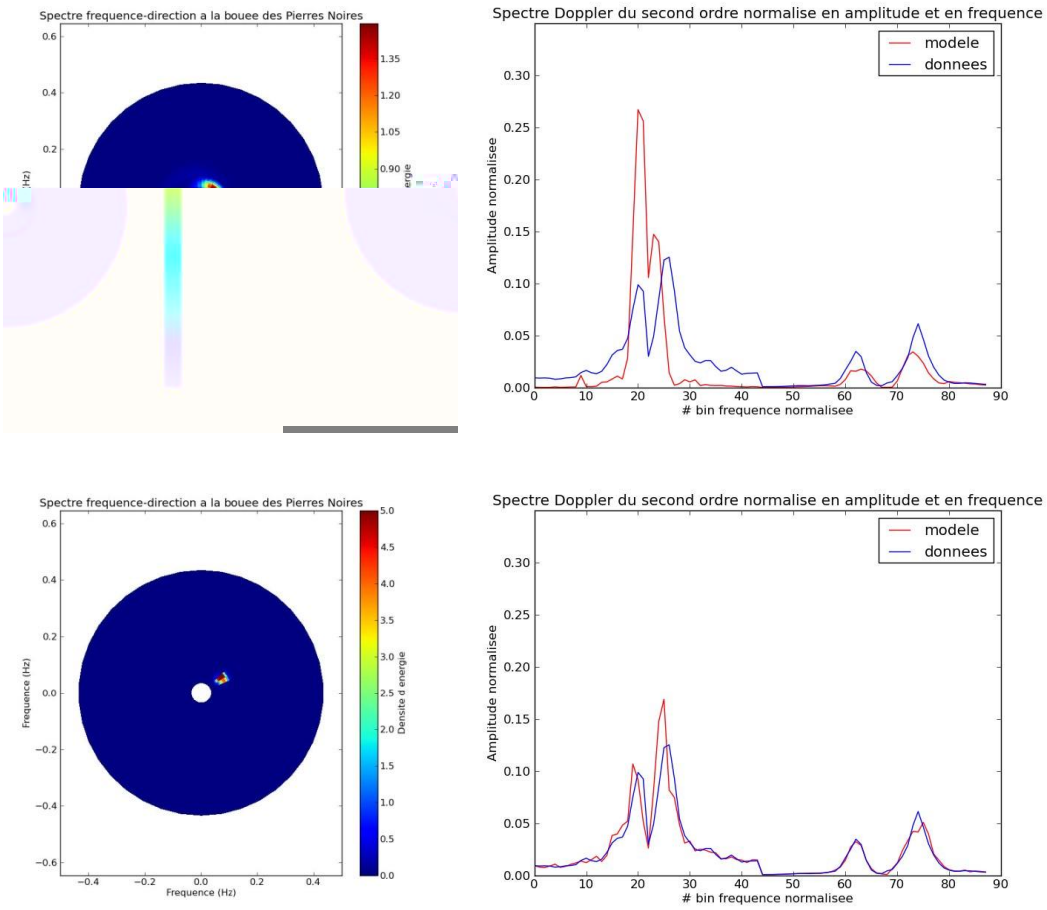

Figure 75 : Wave spectra and second order Doppler spectra on October 14th 2009 03:00 - "Les Pierres Noires". Initial model (upper plot), final model after inversion (lower plot)

For this comparison, the omnidirectional wave spectra were computed (Figure 71). Hs was derived from these spectra (Figure 72).

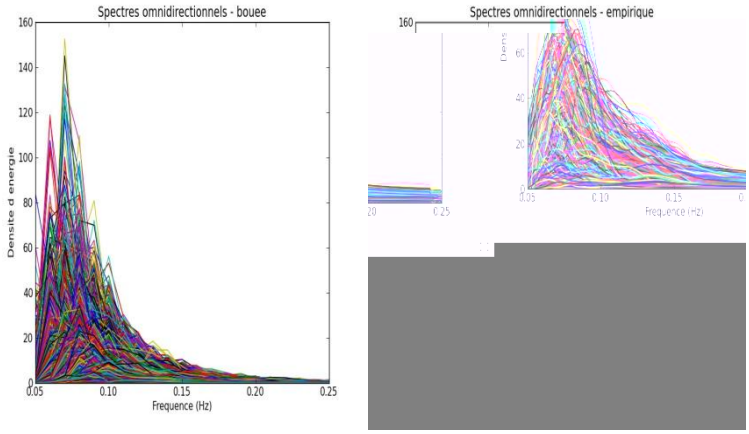

Figure 76 : Omnidirectional spectra over the period October 2009 - December 2009, "Pierres Noires" wave buoy (left), modified empirical method (center), linearized inversion SeaView (right).

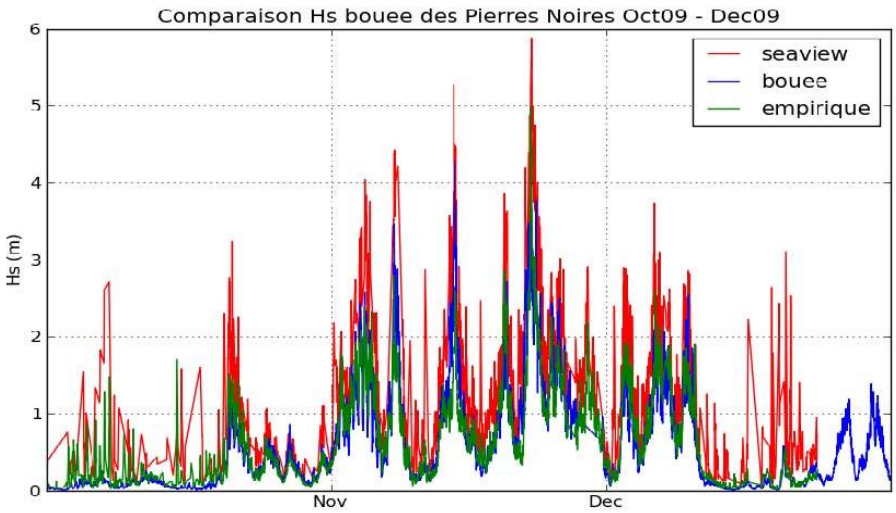

Figure 77 : Significant wave height over the period October 2009 - December 2009, "Pierres Noires" wave buoy, modified empirical method, linearized inversion SeaView.

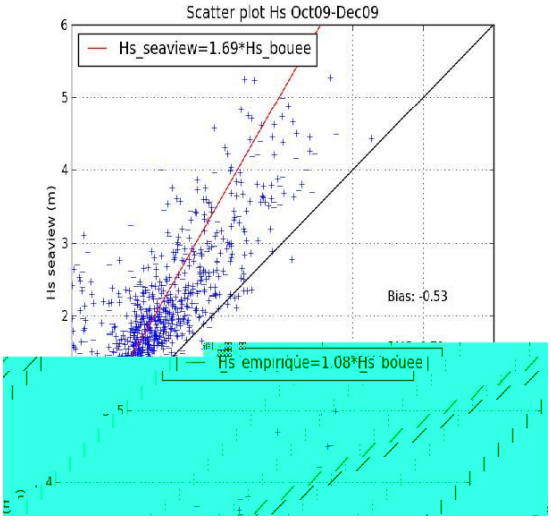

Figure 78 : Significant wave height at the "Pierres Noires" location - comparison between linearized method and in-situ measured data

Hs derived from the adapted empirical method are in rather good agreement with the wave buoy data. Hs assessed using the linearized inversion method show a bias of about 50 cm, an RMS error of about 30 cm and a linear coefficient of 1.69. The agreement is not as good.

Peak period can also be derived from the omnidirectional spectra and are plotted Figure 75.

The distribution of the data observed in the scatter plots and Q-Q plot is due to the frequency sampling.

Results provided by the two methods cannot be considered satisfactory even if the modified empirical method provides a better estimate of the peak periods especially for the longer periods.

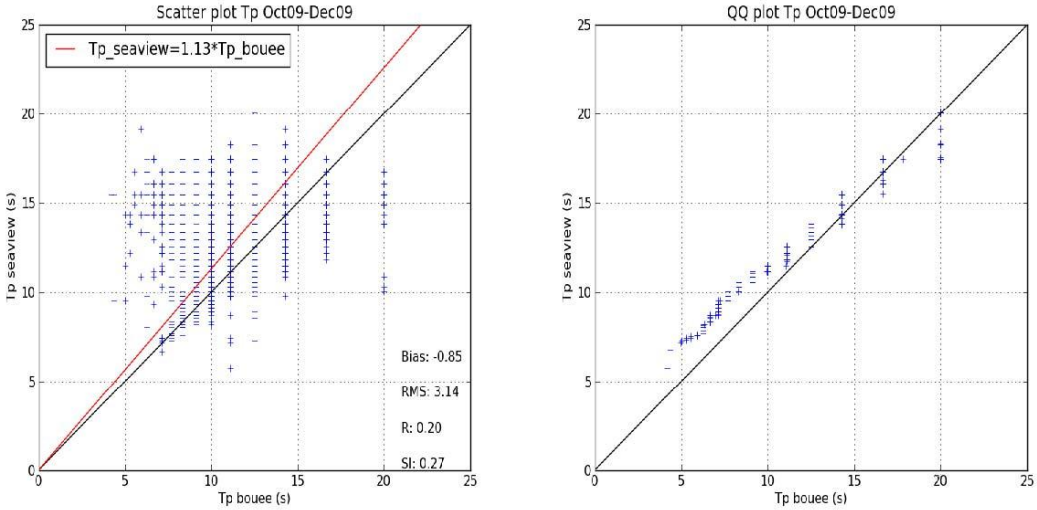

Figure 81 : Peak period at the "Pierres Noires" location - comparison between linearized method and in-situ measured data

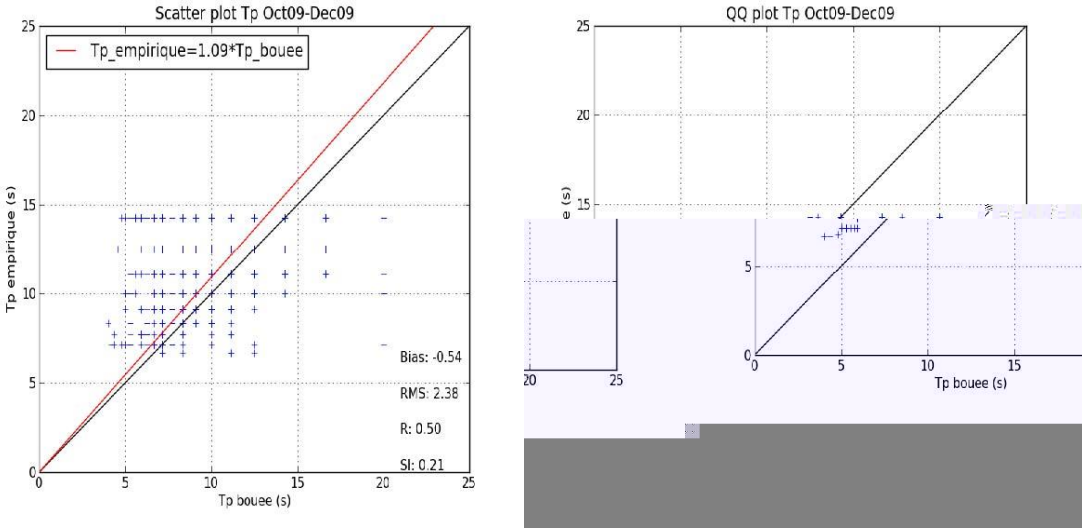

Figure 82 : Peak period at the "Pierres Noires" location - comparison between modified empirical method and in-situ measured data

3.2 Statistics of significant wave height measured by HF radar in the Iroise Sea

Results presented in this chapter were obtained from processing of the HF radars data using the modified empirical method.

3.2.1 Data pre-processing

3.2.1.1 HF radar sea-states data

The covered geographical area is comprised between 47Á20ôN and 49Á20ôN in latitude and -06Á45ôW and -04Á30ôW in longitude. Statistics were built using data sets covering the period from October 2009 to June 2011 with a 30 minutes time step (638 days corresponding to 30624 time steps).

Presented on the map figure 78 are the numbers of valid Hs data per pixel. The maximum number of valid values per pixel is 22941. Among the pixels having data 13% cover slightly less than the total assessment period (about 10000 data per pixel) and only 2.4 % cover 2/3 of the time (> 20000 data per pixels)

Parameter	Number of pixels with N>0	Number of pixels with N>10000	Number of pixels with N>15000	Number of pixels with N>20000
Hs	4257 (100 %)	577 (13.6 %)	307 (7.2 %)	102 (2.4 %)

Table 1: Numbers of data per pixels on the 110X80 radar grid

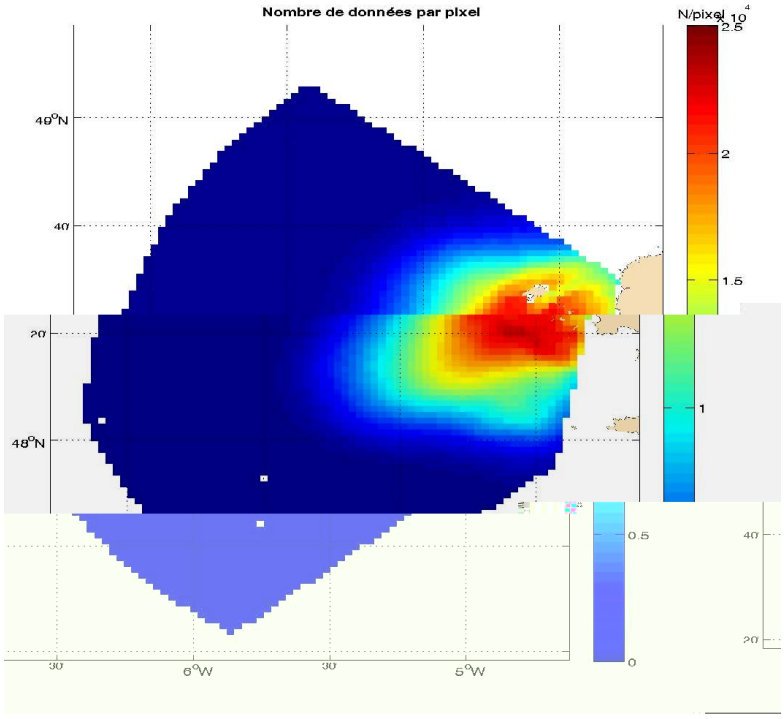

Figure 83 : number of valid Hs data per pixel

3.2.1.2 Masking

The algorithm used for the processing is sensitive to the noise in the radar signal, especially in the areas at the limit of the radar range and in the vicinity of the islands. As a consequence, a mask is built so as to improve the quality of the statistics. Three criteria are selected to build the mask and eliminate the data with the most noise :

- Pixels with a number of available data is lower than 15000 (50%)
- Grid points with strong space/time current gradient
- Pixels where the mean Hs value over the year 2010 is larger than 3.5 m are removed.

The reason for the second criteria is that strong current gradients induce a spreading of the first order Bragg rays that will make difficult the identification and segmentation of the second order components of the Doppler spectrum. When this is the case, the Hs is often overestimated. The masked areas are then defined by comparison of the raw Hs value and data filtered using a moving average filter (over a half tidal cycle, about 6 hours). Areas

where the mean difference between the raw data and the filtered data is too high (>0.7) are masked (figure 79).

The mask based on the two first criteria is presented figure 80. Even when applying these two criteria, high values of the average significant wave height (about 3.5 m) can still be observed in some areas at the limit of the range or in the shadowed area behind Ushant island. In order to compensate for this, the 3rd criterion is applied.

The global mask is presented figure 81. After such processing only 5.9 % of the pixels are saved for the statistical analysis.

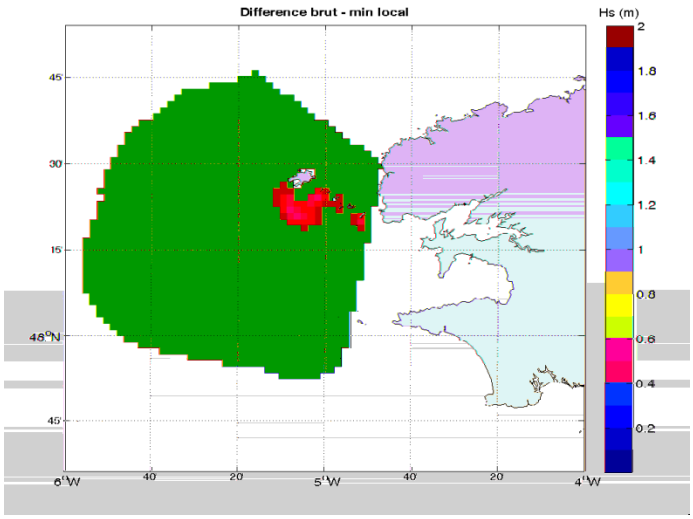

Figure 84 : Mean difference between raw data and filtered data

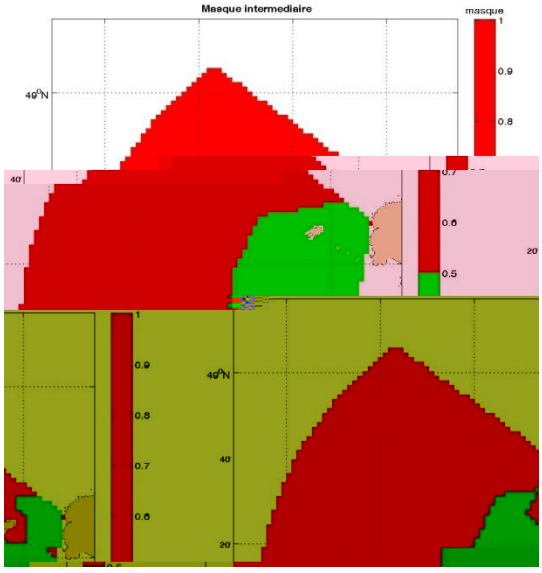

Figure 85 : Mask based on two first criteria (red pixels are removed) (left). Average Hs for the year 2010 (right)

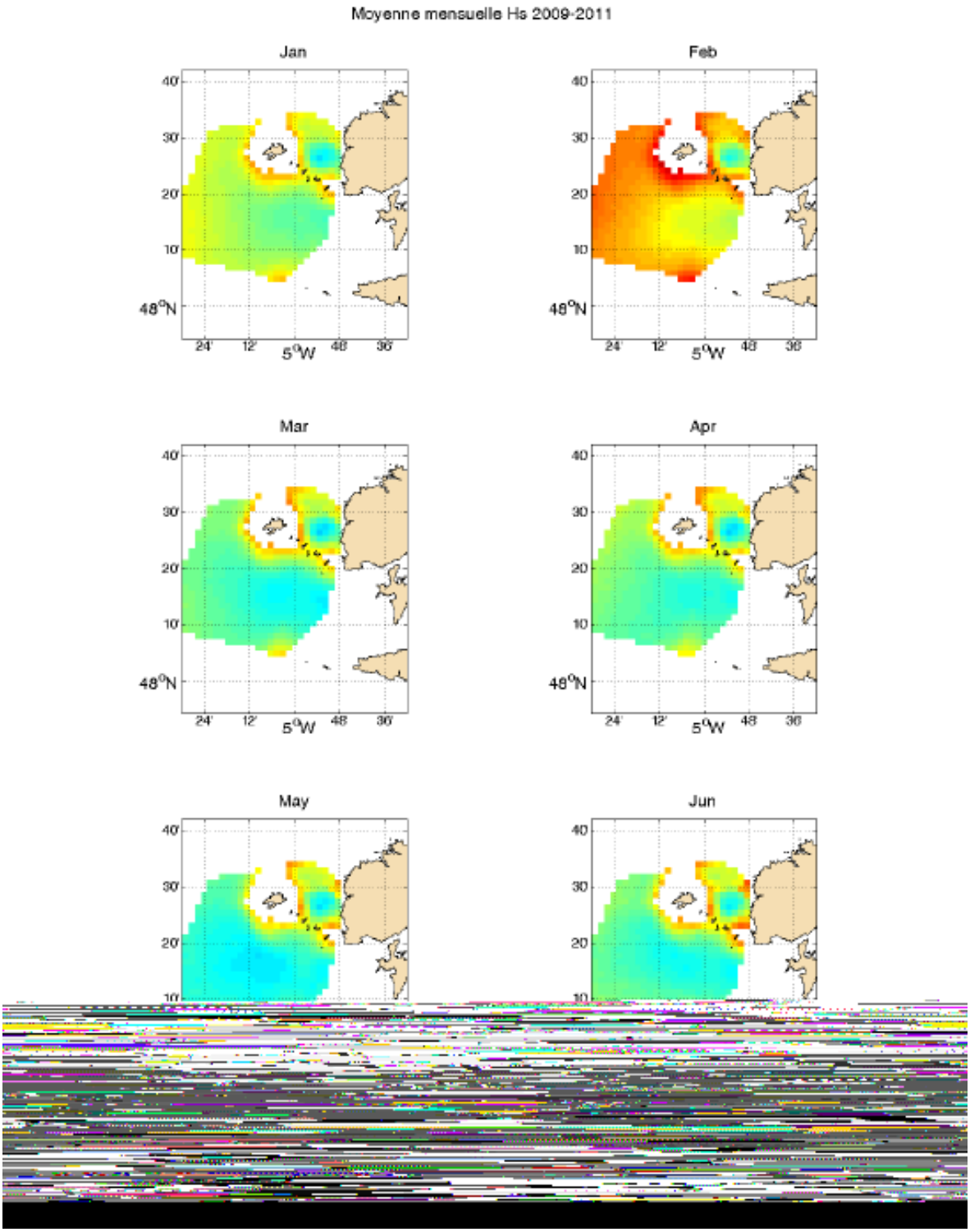

Figure 89 : Hs monthly means for months January to June (October 2009 - June 2011)

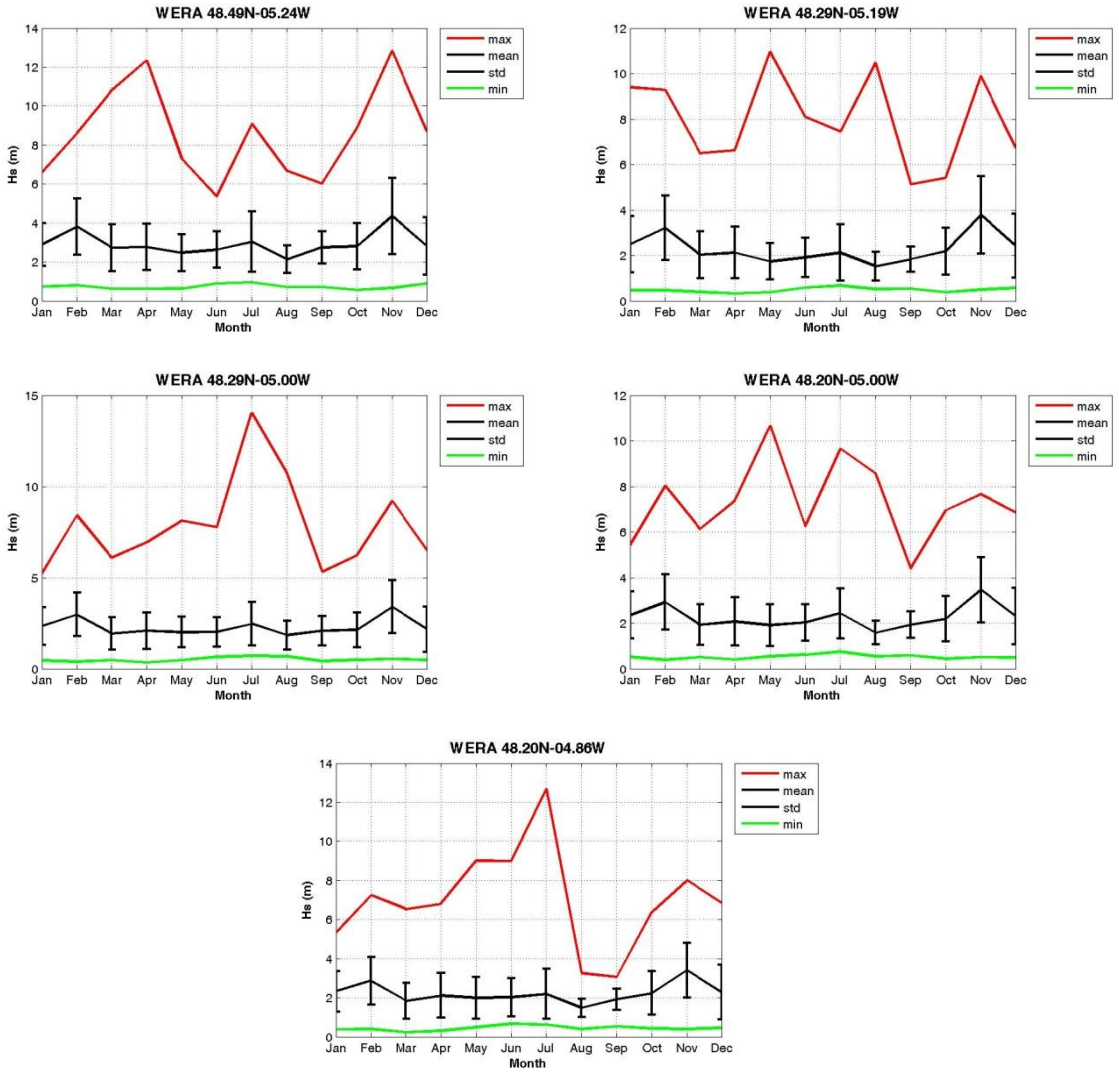

Figure 93 : Hs monthly statistics for the 5 control points

3.3 Statistics of significant wave height measured by HF radar in the Celtic Sea.

3.3.1 Data pre-processing

3.3.1.1 HF radar sea-state data

The radar system described in section 3.1.2.4 operates at a centre frequency of 12 MHz, and makes independent measurements for 17 minutes every hour. These measurements are then used to generate maps of Hs on a 75-by-90 grid at a 1 km resolution. This measuring grid covers an area covering 50Á12.94ôN to 51Á10ôN in latitude and between 05Á5.03ôW and 06Á8ôW in longitude. The dataset used to calculate the statistics presented in this section corresponds to 19 monthsôworth of data, from March 2011 to September 2012, a period equivalent to 580 days and 13,920 time steps.

Depicted in Figure 94 is the percentage of the time each pixel in the grid has valid data. The maximum number of valid values is 11,428, which is 2492 time steps less than the total.

1864 pixels provided valid data more than the 50% of the time and 1440 pixels provided valid data for more than 80% of the time.

Table 2: Number of data per pixel over the 90x75 radar grid

Parameter	Number of pixels with N>0	Number of pixels with N>5714	Number of pixels with N>8571
Hs	6513 (96.49%)	1864 (27.6%)	1440 (21.33%)

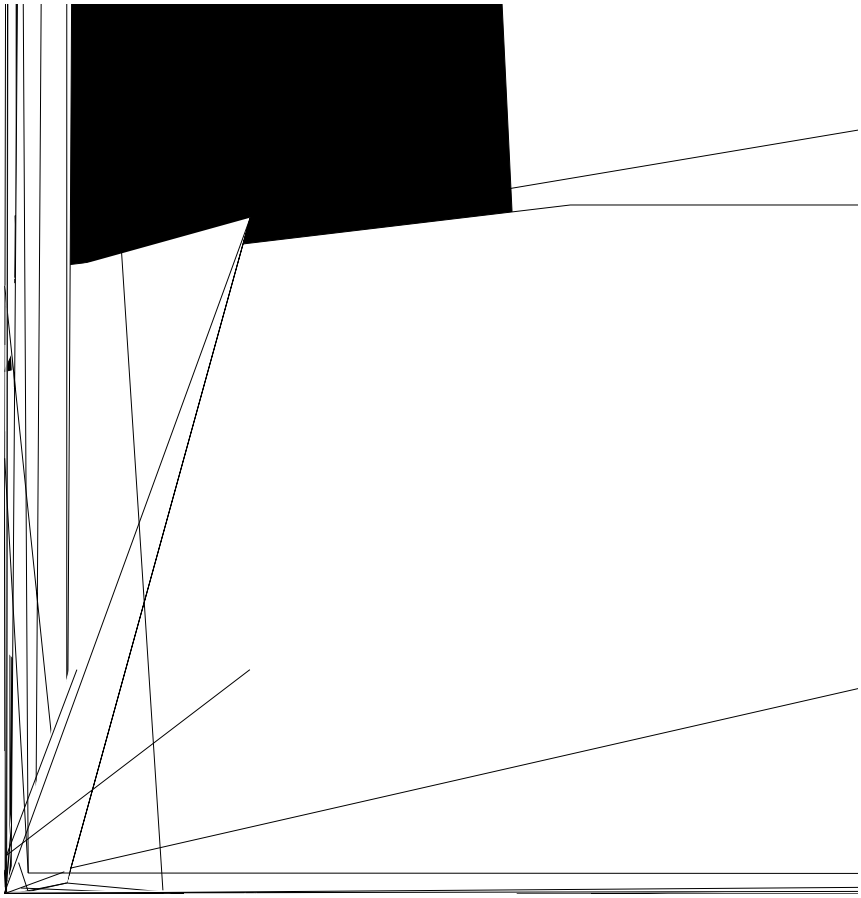

Figure 94: Percentage of valid data per pixel

3.3.1.2 Masking

As mentioned in section 3.2.1.2, the algorithm used for processing is sensitive to the noise in the radar signal. This noise is higher the further one moves on the measuring grid from the radar stations, where the signal to noise ratio is often not enough for the wave information to be accurately extracted from the second order sidebands of the Doppler spectra. Nevertheless, there are times when this ratio is just enough and the algorithm provides wave information at those pixels. However, this information is often neither reliable nor representative to be included in the statistical calculations. Therefore, those pixels where data availability is less than 70% have been removed for subsequent analyses (Figure 95).

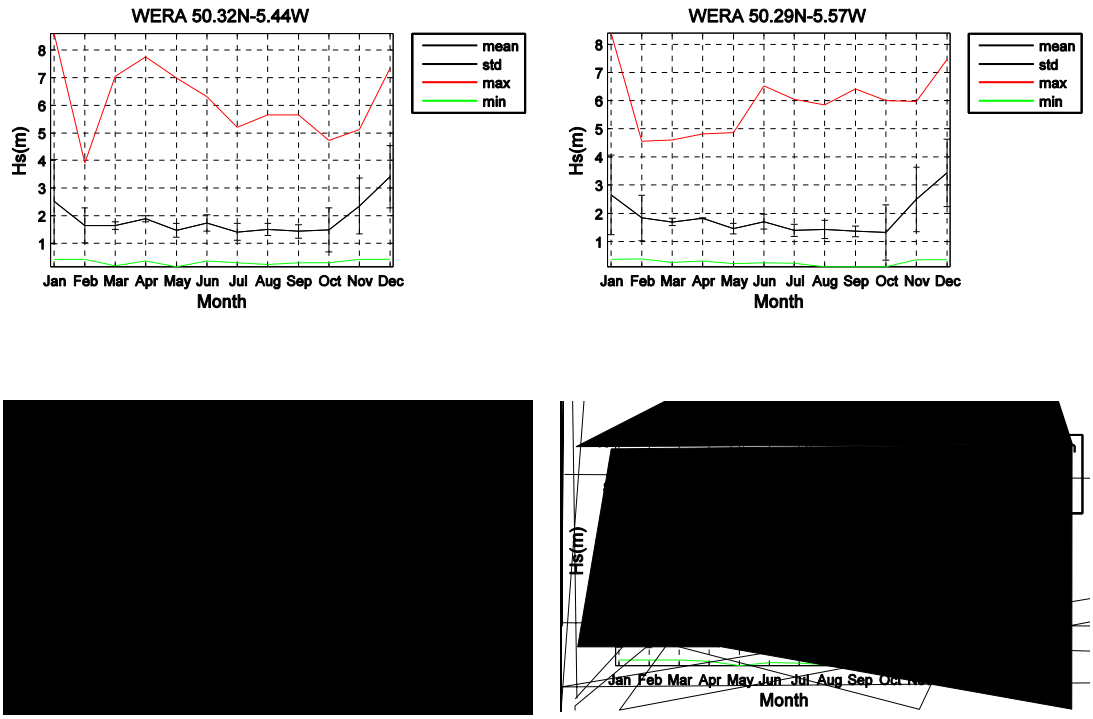

Figure 102: Hs monthly statistics for the 5 control points.

Similarly to the results presented in the figure depicting the mean wave height over the whole grid, the histograms in figure 101 show that most of the time the wave heights are around 2 ï 3 m. The same result can be observed in Figure 102 (black line). The latter figure also shows that February, October, November and December are the months with the highest variability (see standard deviation bars). The maximum wave heights occur on January and December and peaks appear also around May and June. Nevertheless, and as previously mentioned in section 3.2.2.1, these maximum values have to be considered with caution because, even after discarding the values which exceeded 3 standard deviations from the mean of four neighboring points in time, some overestimates may have remained in the dataset.